

Semi-supervised standardized detection of extrasolar planets

S. Sulis¹, D. Mary², L. Bigot², and M. Deleuil¹

¹ Université Aix Marseille, CNRS, CNES, LAM, Marseille, France
e-mail: sophia.sulis@lam.fr

² Université Côte d’Azur, Observatoire de la Côte d’Azur, CNRS, Lagrange UMR 7293, CS 34229, 06304, Nice Cedex 4, France

accepted in A&A

ABSTRACT

Context. The detection of small exoplanets by the radial velocity (RV) technique is limited by various, not well known, noise sources of instrumental and stellar origin. As a consequence, current detection techniques often fail to provide reliable estimates of the “significance levels” of detection tests in terms of false alarm rates or of p -values.

Aims. We aim at designing a RV detection procedure that provides reliable p -values estimates while accounting for the various noise sources typically affecting RV data. The method should be able to incorporate ancillary information on the noise (e.g., stellar activity indicators), and specific data- or context-driven data (e.g., instrumental measurements, magneto-hydrodynamical simulations of stellar convection, simulations of meridional flows or magnetic flux emergence).

Methods. The detection part of the procedure uses a detection test applied to a standardized periodogram. Standardization allows for an autocalibration of the noise sources with partially unknown statistics (Algorithm 1). The part regarding the estimation of the p -value of the test output is based on dedicated Monte Carlo simulations allowing to handle unknown parameters (Algorithm 2). The procedure is versatile in the sense that the specific couple (test, periodogram) is chosen by the user. Ancillary or context-driven data can be leveraged if available.

Results. We demonstrate by extensive numerical experiments on synthetic and real RV data from the Sun and α CenB that the proposed methodology allows to robustly estimate the p -values. The method also provides a way to evaluate the dependence on modeling errors of the estimated p -values attributed to a reported detection, which is a critical point for RV planet detection at low signal-to-noise ratio. The python algorithms developed in this work are available on GitHub.

Conclusions. Accurate estimation of p -values in the case where unknown parameters are involved in the detection process is an important yet newly addressed question in the field of RV detection. Although this work presents a method to this aim, the statistical literature discussed in this paper may trigger the development of other strategies.

Key words. < Techniques: radial velocities - stars: activity - Planets and satellites: detection - Methods: statistical >

1. Introduction

When analyzing Radial Velocity (RV) time series, exoplanets detection tests aim at deciding whether the time series contains one or several planetary signatures plus noise (the alternative hypothesis, noted \mathcal{H}_1), or only noise (the null hypothesis, noted \mathcal{H}_0). With the recent advent of very stable and high precision spectrographs (Pepe et al. 2010; Jurgenson et al. 2016), instrumental noise has reached so low levels (Fischer et al. 2016) that the noise generated by stellar activity has become the limiting factor for the detection of Earth-like planets. Stellar noise is frequency dependent (“colored”) because stellar variability results from several phenomena that contribute simultaneously to the observations and evolve at different timescales. The main stellar noise sources identified so far include magnetic cycles, starspots, faculae, inhibition of the convective blueshift by plagues, meridional circulation, and convective motions of the stellar atmosphere (granulation, supergranulation), and acoustic oscillations. The overall stellar noise affects the frequency range where planets can be found and may dominate the ~ 10 cm/s amplitude level that is typical of an Earth-like exoplanet orbiting a Sun-like star at 1 AU.

The development of techniques to mitigate stellar activity for exoplanet study is an active field of research. Several methods and tools have been developed to account for these different sources in the RV time series (see Meunier (2021) for a re-

cent review). First, some specific observation strategies are commonly used to reduce the contribution of the short timescale activity components (Hatzes et al. 2011; Dumusque et al. 2011). Second, to correct for variability evolving at the stellar rotation period (spots, plagues), the most basic technique consists in fitting a model to the RV dataset (e.g., sinusoidal functions at the stellar rotation period (Boisse et al. 2011), or quasi-periodic Gaussian processes (see e.g. Aigrain et al. 2012; Baluev 2011; Baluev 2013b; Rajpaul et al. 2015; Jones et al. 2022; Rajpaul et al. 2021)). To constrain the parameters of these models, activity indicators (e.g., S-index (Wilson 1968), $\log R'_{\text{HK}}$ (Noyes et al. 1984), bisector span (Queloz et al. 2001)) are commonly used if correlations with the RV dataset are found. Some relations with photometry (Aigrain et al. 2012; Yu et al. 2018), or the study of the chromatic dependence of the stellar activity (Meunier et al. 2017; Tal-Or et al. 2018; Dumusque 2018) can also be used. Recent advances on RV extraction processes from stellar spectra are in particular very promising (Davis et al. 2017; Collier Cameron et al. 2021; Cretignier et al. 2021; de Beurs et al. 2020).

However, despite the diversity of existing techniques to reduce the stellar noise, the presence of residual noise sources at unknown levels translates into uncertainties regarding the interpretation of the RV detection tests. In practice, it is difficult to provide a reliable estimation of the “significance level” of a reported detection. For this reason, examples of debated detection

are numerous (see as examples among others the cases of HD 41248 b and c (Jenkins & Tuomi 2014; Santos et al. 2014), HD 73256 b (Udry et al. 2003; Ment et al. 2018), AD Leo b (Tuomi et al. 2018; Carleo et al. 2020), Aledbaran c (Hatzes et al. 2015; Reichert et al. 2019), or Kapteyn b and c (Anglada-Escudé et al. 2014; Bortle et al. 2021)). As an example, we discuss at the end of this paper the particular case of α CenBb, a debated detection of an Earth-mass planet (Dumusque et al. 2012; Hatzes 2013; Rajpaul et al. 2016; Toulis & Bean 2021).

The main question addressed by the present paper is the evaluation of reliable “significance levels” of detection tests in presence of unknown colored noise. Significance levels are often interpreted through analyses of false alarm probabilities (FAP) or of p -values. The formers are fixed before conducting the tests while the latter measure a “degree of surprise” of the observed test statistic under the null hypothesis. In this work we consider p -values, on the estimation of which a large literature exists in the case where the noise model contains several unknown parameters (Bayarri & Berger 2000). Connections of our approach with the literature are discussed in Sec. 3.3. Accurate estimation of p -values is critical for designing reliable detection methods of small planet RV signatures.

Because the sampling grid is irregular, RV detection is most often performed through the Lomb-Scargle periodogram (LSP; Scargle 1982) or periodograms’ variants (see e.g., Ferraz-Mello 1981, Cumming et al. 1999, Cumming 2004, Reegen 2007, Bourguignon et al. 2007, Zechmeister & Kürster 2009, Baluev 2013a, Jenkins et al. 2014, Tuomi et al. 2014, Gregory 2016, Hara et al. 2017, Hara et al. 2022). While the marginal distribution of periodograms’ components at each frequency is often known for a White Gaussian noise (WGN) of known variance (e.g., a χ^2 distribution for the LSP), the joint distribution of the periodogram components is much more difficult to characterize because the components exhibit dependencies dictated by the sampling grid (or equivalently, by the spectral window).

In practice, specific noise models are applied to correct RV data from the activity, and the p -values of the test statistic are evaluated on the RV residuals assuming they follow the statistics of a WGN, or they have a known covariance matrix.

When the noise is considered WGN, some methods are based on approximate analytical expressions (Baluev 2008). Other methods compute FAP using the formula that would be obtained in the case of independent components, where an ad hoc number of “independent frequencies” is plugged in (see Horne & Baliunas 1986, Schwarzenberg-Czerny 1998, Cumming 2004, as well as Süveges 2014 and Süveges et al. 2015 for a critical analysis of this approach). Finally, another family of approaches is based on Monte Carlo or bootstrap techniques (Paltani 2004, Schwarzenberg-Czerny 2012), possibly aided by results from extreme values distribution (Süveges 2014, Süveges et al. 2015).

In a large majority of cases, however, the noise in RV residuals is not white but colored with unknown power spectral density (PSD). In this situation, providing reliable FAP estimates remains, to our knowledge, an open problem. Indeed, assuming the noise PSD is flat leads logically to increased false alarms in the PSD bumps, and to a loss of detection power in the PSD valleys (e.g., see Fig. 2 in Sulis et al. 2016). This problem is only partially solved in practical approaches where a covariance model is fitted to the data and used to produce residuals that are assumed to be white. For instance, Delisle et al. (2020) recently presented an analytical formulation of the p -value resulting from the generalization of Baluev (2008) to the case of colored noise when the covariance matrix is known. Their results

indicate that the FAP estimates are highly dependent on the considered covariance matrix, with variations directly related to the mismatch between the true and assumed covariance matrix. Similar effects were analyzed in Sulis et al. (2016) and in Sec. 3.5 of Sulis (2017). To our knowledge, all methods aimed at evaluating the FAP or p -values associated with periodogram tests assume that the noise is eventually white, either directly or because the model used for the covariance is considered exact, so that the signal can be whitened. Since estimation errors in the noise statistics lead to fluctuations in the p -value estimates, our incomplete knowledge of the noise sources and their statistics represents a fundamental limitation to how much we can trust these estimates. The present work deals precisely with this problem. Another critical point is the consistency of the p -values estimate when different noise models are used in the detection process (this point was very clearly raised by Rajpaul et al. 2016 for instance). The controversy about low-mass planets detection often resides in the different noise models that are assumed for the data. Since i) noise models can never be exact and ii) estimated p -values are model-dependent, incorporating model errors in their estimations appears as a relevant (yet new) approach and we follow this path below.

In this paper, we propose a new RV planet detection procedure that can generate reliable estimates of the “significance levels” of detection tests, by means of p -values. The approach is built on a previous study (Sulis et al. 2020), which was limited to the case of regularly sampled time series and primarily considered the effect of granulation noise. Both of these limitations are removed in the present paper.

The approach is flexible and can deal with the main characteristics encountered in practice with RV detection: irregular sampling and various noise sources with partially unknown noise statistics. The basic principle of the procedure is to propagate errors on the noise model’s parameters to derive accurate p -values of detection tests by means of intensive Monte Carlo simulations. The choice of the noise models involved in the procedure is entirely left to the user, as well as the choice of the periodogram and detection test. We note that, without loss of generality, the procedure can be applied to RV dataset resulting from any extraction process (including for instance the extraction techniques recently described in Collier Cameron et al. 2021 or Cretignier et al. 2021). In addition, the procedure can exploit training time series of stellar or instrumental noise, if such data is available, for instance through auxiliary observations or realistic simulations.

The core of the new detection approach is presented in Sec 2 (Algorithm 1). The numerical procedure for estimating the p -values of the test statistic produced by Algorithm 1 is presented in Sec 3 (Algorithm 2). Validations of the p -values estimation procedure under different configurations are given in Sec. 4 and 5. We conclude with the application of the detection procedure on the RV data of α CenB, where an Earth-mass planet detection has been debated (Sec. 6). In this last section, we show how the proposed detection procedure can be used to evaluate the robustness of a planet detection with respect to specific model errors. Examples of how to use the algorithms developed in this work are available on GitHub¹, and practical details are given in Appendix. A.

¹ <https://github.com/ssulis/3SD>

2. Semi-supervised standardized detection

A word on the notations: bolded small (resp. capital) letters with no subscript indicate column vectors (resp. matrices). Vector (resp. matrix) components are denoted by subscripts. For instance we write vector \mathbf{x} as $\mathbf{x} = [\mathbf{x}_1, \dots, \mathbf{x}_N]^\top$. We denote by \hat{z} the estimate of a quantity z . Throughout the paper the notation $|$ means “conditional on” (and it is not necessarily used for probability densities). Appendix B summarizes the main notations of this work.

2.1. Hypothesis testing

Consider a RV time series under test, \mathbf{x} , irregularly sampled at N time instants $\mathbf{t} = [t_1, t_2, \dots, t_N]^\top$. Our detection problem can be cast as a binary hypothesis problem of the form:

$$\begin{cases} \mathcal{H}_0 : \mathbf{x} = \mathbf{d} | \mathcal{M}_d(\theta_d) + \mathbf{n}, \\ \mathcal{H}_1 : \mathbf{x} = \mathbf{s} | \mathcal{M}_s(\theta_s) + \mathbf{d} | \mathcal{M}_d(\theta_d) + \mathbf{n}. \end{cases} \quad (1)$$

The signal \mathbf{d} accounts for various effects that usually affect RV data. A non-exhaustive list of such effects includes long term instrumental trends, stellar magnetic activity, or RV trends due to additional companion in the system. This nuisance signal, which is the unknown mean under \mathcal{H}_0 , cannot be estimated by numerical simulations. While \mathbf{d} can be of random origin, it is customary to model it as a deterministic signature (see, e.g., Dumusque et al. 2012). This is our approach in the following. We shall refer to \mathbf{d} as a nuisance signal and write generically that \mathbf{d} is generated from some model \mathcal{M}_d with parameters θ_d .

The noise $\mathbf{n} \sim \mathcal{N}(\mathbf{0}, \Sigma)$ is a zero mean stochastic noise of unknown covariance matrix Σ that we decompose into

$$\Sigma = \Sigma_c + \Sigma_w, \quad (2)$$

with Σ_w a diagonal covariance matrix whose entries account for possibly different uncertainties on the RV measurement. If those are equal, $\Sigma_w = \sigma_w^2 \mathbf{I}$ with σ_w^2 the variance of a WGN (noted \mathbf{w} below), and Σ_c the unknown covariance matrix of a colored noise². A non-exhaustive list of effects that can be included in \mathbf{n} entails meridional circulation, magnetic flux emergence, stellar granulation, supergranulation, instrumental noise. The choice of which type of RV noise component fits in \mathbf{d} or \mathbf{n} depends on the assumptions made by the user about the RV time series under test.

Under the alternative hypothesis (planet(s) present), the time series \mathbf{x} contains the same noise components \mathbf{d} and \mathbf{n} plus a deterministic signal \mathbf{s} corresponding to the Keplerian signatures of planets (model \mathcal{M}_s). The number of planets and their Keplerian parameters θ_s are unknown.

Throughout this paper, we will consider the optional case where context-driven data of the stochastic colored noise \mathbf{n} in (1) can be made available for instance through realistic simulations. We call this data the null training sample (NTS)³.

For example, focusing on the stellar granulation noise, Sulis et al. (2020) showed that 3D magneto-hydrodynamical (MHD) simulations can generate realistic synthetic time series of this

RV noise source (see also Appendix C). This was also demonstrated in Palumbo et al. (2022) with synthetic stellar spectra simulators. This suggests that using simulations of stellar granulation in the detection process could provide an alternative to the observational strategy of binning spectra over a night (Dumusque et al. 2011). Indeed, Meunier et al. (2015) and Meunier & Lagrange (2019) showed that while convection (granulation and supergranulation) dominates at high frequencies, where it acts as a power law noise ($\sim 1/f$), convection has energy at all frequencies so that averaging on short timescales is not efficient enough to detect RV signatures of Earth-like planets hidden in the convection noise.

Other examples where NTS can be obtained is from 3D MHD simulations of stellar supergranulation (e.g. Rincon & Rieutord 2018), empirical simulations of stellar meridional flows (Meunier & Lagrange 2020), or specific data-driven observations representative of the “instrumental noise” (e.g., micro-telluric lines Cunha et al. 2014 Seifahrt et al. 2010) affecting the RV data. In general, all realistic synthetic time series of the stochastic colored noise sources affecting the RV data can be included in the NTS.

This setting poses a general question: how could such a NTS be leveraged to improve the detection process, both in terms of detection power and of the accuracy of the computed p -value? Such an approach was proposed and analyzed in Sulis et al. (2017a) but with $\mathbf{d} = \mathbf{0}$ and a regular sampling for \mathbf{x} in model (1). In this approach, the detection test was automatically calibrated by the NTS through a standardization of the periodogram. While this preliminary work has demonstrated improved performances in terms of power and control of the p -value, it presents however two important limitations for RV detection purposes. First, the approach accounts only for noise that can be generated through realistic simulations. Second, the scope was limited to regular sampling. In contrast, the detection procedure proposed below can cope with all components of noise, including instrumental and stellar noises of different origins ($\mathbf{d} \neq \mathbf{0}$) and any type of time sampling. This general procedure is semi-supervised in the sense that it incorporates ancillary sources of noise affecting the data. Since it is also based on a periodogram standardization, we call this procedure semi-supervised standardized detection (3SD for short). The 3SD procedure contains two algorithms: one for detection, one for evaluating the resulting significance levels.

2.2. Periodogram standardization

2.2.1. Case where an NTS is available

We assume that the NTS, if available, takes the form of L sequences of synthetic time series of noise \mathbf{n} in (1):

$$\mathcal{T}_L := \{\mathbf{n}^{(i)}, i = 1, \dots, L, \quad \mathbf{n}^{(i)} \sim \mathcal{N}(\mathbf{0}, \Sigma). \quad (3)$$

An efficient way to leverage such side information in the detection process is to compute standardized periodograms (see Sulis et al. 2020). Let Ω denote the set of frequencies at which the periodogram, noted \mathbf{p} , is computed (Ω and the type of periodogram \mathbf{P} are defined by the user). We note ν_k these frequencies and N_Ω their number. The periodograms of each of the L series of the NTS, $\mathbf{p}_\ell(\nu_k)$, with $\ell = 1, \dots, L$, can be used to form an averaged periodogram, $\bar{\mathbf{p}}_L(\nu_k)$, as the sample mean of these L periodograms:

$$\bar{\mathbf{p}}_L(\nu_k) := \frac{1}{L} \sum_{\ell=1}^L \mathbf{p}_\ell(\nu_k). \quad (4)$$

² Here, Σ_c is considered fixed. Temporal variations of Σ_c as the ones considered by Balu (2015) could in principle be considered by our numerical procedure by sampling according to a time-dependent covariance structure, but this is left out of the scope of the present paper.

³ By construction, this NTS is free from any possible “contamination” by the planetary signal.

The standardized periodogram is then defined as:

$$\tilde{\mathbf{p}}(\nu_k) := \frac{\mathbf{p}(\nu_k)}{\bar{\mathbf{p}}_L(\nu_k)}. \quad (5)$$

In the following, \mathbf{p} and $\bar{\mathbf{p}}_L$ denote the vectors concatenating the periodograms ordinates at all frequencies in Ω and the standardized periodogram is noted $\tilde{\mathbf{p}} \mid \bar{\mathbf{p}}_L$ or simply $\tilde{\mathbf{p}}$.

In the case of regular sampling and when $\mathbf{d} = \mathbf{0}$, Sulis et al. (2020) demonstrated that standardization avoids both a loss of detection power in valleys of the noise PSD, and an increase of the false alarm rate in its peaks (see Sulis et al. (2016), and Sec.3.5.3 of Sulis (2017)). An important point of the present paper is to show that such desirable features also hold in the case of irregular sampling for different models of \mathbf{d} and \mathbf{n} (see Sec. 4 and Sec. 5).

2.2.2. Case where no NTS is available

Simulations (such as 3D MHD simulations of stellar granulation) are computationally demanding and hence generating very long time series (month, years) may appear out of reach for standard RV planet searches. It is also worth mentioning that helioseismology has revealed that 3D MHD simulations are unable to reproduce the power of large scale flows in the Sun (supergranulation), so improvements are still needed in this field of research (Hanasoge et al. 2012). For these reasons, we also consider the case where no NTS of \mathbf{n} in (1) is available. In this case, the periodogram standardization relies on a parametric model \mathcal{M}_n whose parameters are estimated from the RV data⁴. In this approach, synthetic time series of \mathbf{n} are generated and used to compute the averaged periodogram used in (4). Example of stochastic parametric models are numerous, and a (non-exhaustive) relevant list for RV data includes Harvey-like functions (Harvey 1985), autoregressive (AR) models (Brockwell & Davis 1991; Elorrieta et al. 2019), or Gaussian processes (Rasmussen & Williams 2005)).

A particular noise configuration happens when noise \mathbf{n} is white ($\Sigma_c = 0$ leading to $\Sigma = \sigma^2 \mathbf{I}$ in (2)). In this case, the standardization of the periodogram in (5) is simply performed by the estimated variance of the RV time series.

2.3. Considered detection procedure

The detection procedure proposed in this work is described in Fig. 1. We will refer to this procedure as “Algorithm 1” in the following.

The first step (rows 1 to 4) aims at computing the periodogram \mathbf{p} involved in (5). For this purpose, if the nuisance component \mathbf{d} is present in model (1), the algorithm starts by removing it from the time series \mathbf{x} by fitting model \mathcal{M}_d (blue block). The residuals are used to compute \mathbf{p} (row 4). If $\mathbf{d} = \mathbf{0}$ is not present in (1), then the blue block is ignored and we directly compute \mathbf{p} with the data under test (\mathbf{x}).

Note that, in this first step, the Algorithm removes the nuisance signals and detection is performed on the residuals. A more general detection approach, as the Generalized Likelihood Ratio approach (Kay 1998), would require estimating jointly all unknown parameters under both hypotheses. Such an approach would lead to different nuisance parameters under \mathcal{H}_0 and \mathcal{H}_1 , since the parameters of the nuisance signals are consecutively

⁴ When a NTS is available, model \mathcal{M}_n is not necessary for the detection process in Algorithm 1, this is why it was not made explicit in model (1).

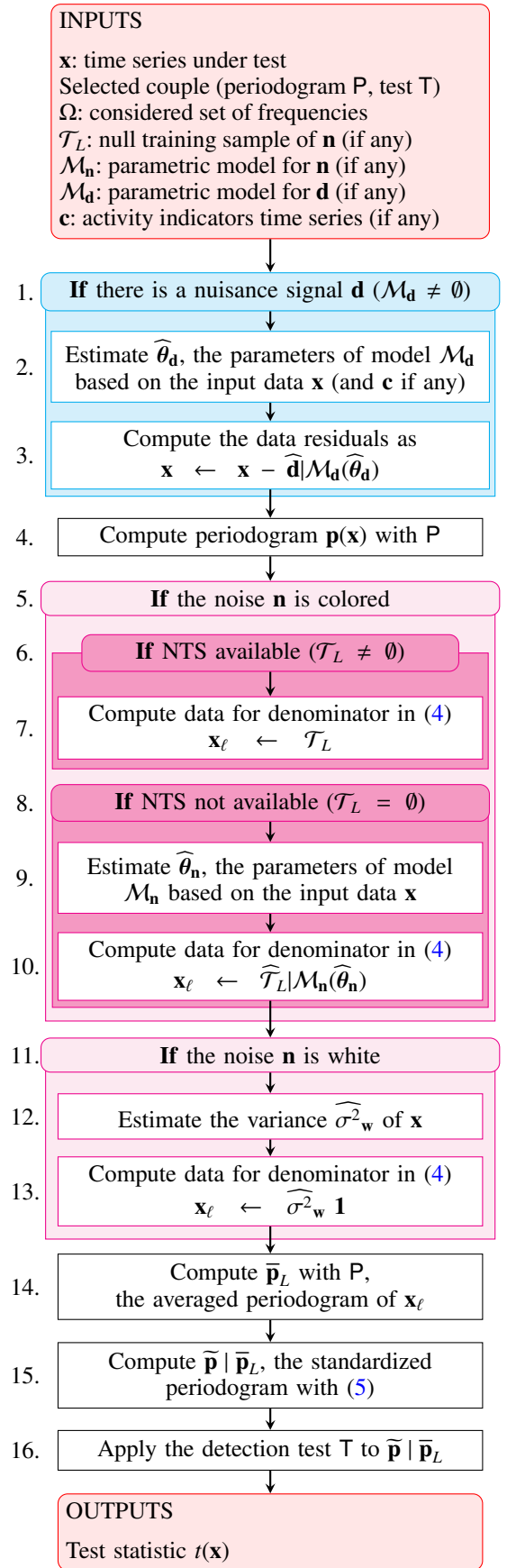


Fig. 1: Detection part of the 3SD procedure (Algorithm 1).

estimated with or without those of the signal (sinusoidal or Keplerian parameters). This procedure can however be computation-

ally very heavy – or even intractable – when Maximum Likelihood Estimation is required over a large number of parameters. Hence, it is discarded in our framework where nuisance parameters are estimated only under \mathcal{H}_0 . Note that in the case of weak planetary signatures, the perturbation of these signatures on the nuisance parameters is weak, so that the estimation of these parameters does not change much under both hypotheses.

The second step (rows 5 to 10) aims at computing the averaged periodogram $\bar{\mathbf{p}}_L$ involved in (5). For this purpose, if \mathbf{n} in (1) is a colored noise for which an NTS is available (rows 6 to 7), we take directly the L null training series to compute $\bar{\mathbf{p}}_L$ in row 14. If no NTS is available (rows 8 to 10), we fit model $\mathcal{M}_{\mathbf{n}}$ to the time series under test \mathbf{x} and compute a synthetic NTS (called $\widehat{\mathcal{T}}_L$) with the estimated model parameters $\widehat{\boldsymbol{\theta}}_{\mathbf{n}}$. In this case, $\bar{\mathbf{p}}_L$ in row 14 is evaluated after generating a sufficiently large number of synthetic noise time series from $\mathcal{M}_{\mathbf{n}}$. If noise \mathbf{n} is white (rows 11 to 13), the averaged periodogram in row 14 simply becomes the product of the estimated variance of \mathbf{x} , say $\widehat{\sigma}_{\mathbf{w}}^2$, by vector $\mathbf{1} := [1 \dots 1]^\top$.

The final steps of the procedure consist in computing $\widetilde{\mathbf{p}} \mid \bar{\mathbf{p}}_L$ (row 15) and applying the detection test T (row 16). The procedure returns the test statistic $t(\mathbf{x})$.

2.4. Periodogram and test considered in this work

In order to illustrate our detection framework, we will mainly consider in this study the Lomb-Scargle periodogram (Scargle 1982). Hence, both the numerator and the denominator in (5) will be LSP. As for the detection test, we will consider the test whose statistic is the largest periodogram peak. This test will be referred to as “Max test” for short. The Max test statistic writes:

$$T_M(\widetilde{\mathbf{p}} \mid \bar{\mathbf{p}}_L) := \max_k \widetilde{\mathbf{p}}(v_k). \quad (6)$$

We emphasize that the 3SD detection procedure is not tied to the particular choice of the couple (periodogram, test) selected above. It can indeed be applied as such to other types of periodograms and test statistics exploiting differently the periodogram’s ordinates (see Sulis et al. 2016 and Sulis et al. 2017a for examples of other detection tests). Table 1 summarizes examples of input parameters that can be used in Algorithm 1.

Once Algorithm 1 has computed the test statistic of \mathbf{x} , an important question is that of evaluating its p -value. This is the purpose of Sec. 3.

3. Numerical estimation of the p -values

For an observed test statistic t , the p -value is denoted by $p_v(t)$ and defined as

$$p_v(t) := \Pr(T > t \mid \mathcal{H}_0).$$

For example, when all parameters are known, the p -value of a test statistic t obtained by the Max test (6) is defined as:

$$p_v(t) := \Pr(T_M(\widetilde{\mathbf{p}} \mid \bar{\mathbf{p}}_L) > t \mid \mathcal{H}_0) = 1 - \Phi_{T \mid \mathcal{H}_0}(t), \quad (7)$$

with $\Phi_{T \mid \mathcal{H}_0}$ the cumulative distribution function (CDF) of the test statistic under \mathcal{H}_0 .

A p -value estimation procedure to which all parameters of the statistical model are known under \mathcal{H}_0 is called “oracle” in the statistical literature (see Donoho & Johnstone (1994); Roquain & Verzele (2022); Mary & Roquain (2021) and references therein). We describe such an oracle procedure in Sec. 3.1.

When unknown nuisance parameters are present under \mathcal{H}_0 , the computation of p -values is not straightforward. A common

approach allowing to account for uncertainties in the model’s parameters considers the unknown parameters under \mathcal{H}_0 as random and computes the expectation of p -values over a prior parameter’s distribution. This is the approach of the MC procedure proposed in Algorithm 2 (see Sec. 3.2). Connections with existing approaches are discussed in Sec. 3.3.

In practice, a desirable feature of the procedure is also to provide an interval within which the true (i.e., oracle) p -value has a high probability to lie (for instance 90%). The MC sampling approach of Algorithm 2 naturally provides estimates of such intervals, called 90% intervals below. As a complementary p -value estimate, the largest p -value (upper envelope of the sampled p -values) obtained from the simulation can also be used as a (often overly) conservative estimate (Bayarri & Berger 2000). In practice, a large difference between the two estimates is the sign of a large dependence of the estimation results on the considered models and parameters.

3.1. Oracle

When all parameters under the null hypothesis are known, which is of course an ideal situation not met in practice, a straightforward way for evaluating the oracle p -values numerically consists in performing Algorithm 1 a large number of times (say, b) to get a set $\{t(\mathbf{x})\}_{j=1, \dots, b}$ of realizations of the test statistic t . From this set, we can compute an empirical estimate of $\Phi_{T \mid \mathcal{H}_0}$, called $\widehat{\Phi}_T$ for short, and an estimated p -value by plugging $\widehat{\Phi}_T$ in (7). The estimation of the p -value can be made arbitrarily accurate since $\widehat{\Phi}_T$ converges to $\Phi_{T \mid \mathcal{H}_0}$ as $b \rightarrow \infty$.

3.2. Algorithm for estimating the p -values

The generic procedure (Algorithm 2) is presented in Fig. 2. The final expected p -value (\widehat{p}_v) is obtained by sample expectation (row 19) over B p -values $\widehat{p}_v^{(i)}$ obtained in a major loop (green, rows 1 to 18). Each such p -value is obtained through a minor loop (rows 5 to 16) that measures an empirical CDF ($\widehat{\Phi}_T^{(i)}$). Note that this loop (and this estimated CDF) includes an averaging over the priors $\pi_{\mathbf{d}}$ and $\pi_{\mathbf{w}}$.

The major loop samples B values of the parameters for \mathbf{n} ($\widehat{\boldsymbol{\theta}}_{\mathbf{n}}^{(i)}$), which are obtained by parametric bootstrap: a sample NTS is generated according to parameters $\widehat{\boldsymbol{\theta}}_{\mathbf{n}}$ estimated from the data (rows 3 and 4).

In the nested minor loop (blue), the algorithm samples a number b of test statistics t produced by Algorithm 1 conditionally to $\widehat{\boldsymbol{\theta}}_{\mathbf{n}}^{(i)}$ (if \mathbf{n} is colored), $\widehat{\sigma}_{\mathbf{w}}^{(i,j)}$ (if \mathbf{n} is white) and to $\widehat{\boldsymbol{\theta}}_{\mathbf{d}}^{(i,j)}$ (if $\mathbf{d} \neq \mathbf{0}$ in (1)). These parameters values are obtained by randomly perturbing the corresponding input values $\widehat{\sigma}_{\mathbf{w}}^2$ and $\widehat{\boldsymbol{\theta}}_{\mathbf{d}} \mid \mathcal{M}_{\mathbf{d}}$ within reasonable uncertainties according to some prior distributions, named $\pi_{\mathbf{w}}$ (row 10) and $\pi_{\mathbf{d}}$ (row 13). If model $\mathcal{M}_{\mathbf{d}}$ involves the use of an ancillary series \mathbf{c} , a synthetic series $\widehat{\mathbf{c}}^{(i,j)}$ is generated in row 14 using the same models’ parameters $\widehat{\boldsymbol{\theta}}_{\mathbf{d}}$ plus a WGN.

Each test statistic is then obtained by applying Algorithm 1 to simulated time series $\mathbf{x}^{(i,j)}$ (row 16). If \mathbf{n} is colored, Algorithm 1 takes in input the L simulated NTS $\mathcal{T}_L^{(i,j)}$ (computed in row 7) for periodogram standardization. If \mathbf{n} is white, this vector is sent as empty in Algorithm 1.

A particular case of this Algorithm arises when the noise is considered colored with a parametric model $\mathcal{M}_{\mathbf{n}}$ and no NTS is

Table 1: Input parameters used in this work for Algorithms 1 and 2, and non-exhaustive list of additional examples that can be used.

Input parameter	Examples selected in this work for illustration	Other examples
Periodogram P	Lomb-Scargle periodogram (Sec. 4,5,6), Generalized Lomb-Scargle (Sec. 5.5)	Other periodograms' variants: e.g., Ferraz-Mello 1981, Cumming et al. 1999, 2004, Reegen 2007, Bourguignon et al. 2007, Baluev 2013, Jenkins et al. 2014, Tuomi et al. 2014, Gregory, 2016, Hara et al. 2017, 2021
Detection test T	Max test T_M (Eq.(6)), Test of the N_C^{th} largest value, T_C (Eq.(9))	Any detection test (see e.g., in Sulis et al. 2017): e.g., Higher Criticism (Donoho & Jin 2004), Berk-Jones (Berk & Jones 1979)
Noise models \mathcal{M}_d	Gaussian process (Eq.(10)), Linear activity proxy with polynomials (Eq.(14)), Linear activity proxy (Eq.(16))	Any relevant model for \mathbf{d} : e.g., models for long term instrumental trends, stellar magnetic activity, binary trends
Noise models \mathcal{M}_n	AR process (Eq.(8)) Harvey function (Eq.(13))	Any relevant model for \mathbf{n} : e.g., models for meridional circulation, stellar granulation, supergranulation, or instrumental noise
Ancillary time series \mathbf{c}	$\log R'_{\text{HK}}$ (Sec. 5, Sec. 6)	Any activity proxy for \mathbf{d} : e.g., S-index (Wilson, 1968), FF' (Aigrain et al. 2012), bisector (Queloz et al. 2001)

available. This case impacts the setting of L in rows 3 and 7 and is explained in Sec. 5.5.

For π_w and π_d , we consider in the simulations below Gaussian and uniform priors (with independent components if multivariate). The components' distributions are centered on the parameters' values estimated from the data. The scale parameters (widths of the intervals for uniform priors or variances for the Gaussian prior) are estimated from the estimation error bars.

3.3. Connection with the literature

In the statistical literature, several approaches exist for estimating p -values when unknown parameters are involved in the detection process (see Bayarri & Berger 2000 for a review). Among these approaches, prior predictive p -values are obtained by averaging over a prior law of the parameters (Box 1980). In contrast, posterior predictive p -values require to average over the posterior distribution (Guttman 1967; Rubin 1984). Sampling from the posterior would require a computationally involved procedure (with Markov Chain Monte Carlo for instance). For this reason, we do not follow the posterior predictive approach here and aim at keeping the sampling process simple. In our approach, this process is different depending on the parameters we consider:

- Regarding the parameters of \mathcal{M}_n (row 4 of Algorithm 2), which corresponds to a parametric model of a random process, a natural way of sampling parameters over a distribution that is consistent with our model is to sample the random process with the estimate at hand and to re-estimate the parameters. This is what we do here. This approach also avoids choosing an explicit prior for θ_n , of which the parameters would need to be set or estimated.

- As far as the other unknown parameters are concerned (σ_w and θ_d in the rows 10 and 13 of Algorithm 2), we have not used the same strategy for computational reasons. Here, we found it more efficient to sample these parameters from some priors (Gaussian and uniform), whose parameters were estimated from the estimated error bars in an empirical Bayes manner (Efron & Hastie 2016).

The performances of the generic Algorithm 2 are evaluated on real and synthetic data in the three next sections.

4. Noise = Granulation + WGN

4.1. Objectives

We first consider the simplest case where the RV time series is only affected by the stochastic colored noise \mathbf{n} in (1), of which a training set \mathcal{T}_L is assumed available (i.e. we set $\mathbf{d} = \mathbf{0}$ in (1), and $\mathcal{M}_d = \emptyset$ in Algorithms 1 and 2). While this configuration is not realistic for most long period planet RV searches, where magnetic activity phenomena (defined in \mathbf{d}) always play an important role in the observed RV time series, it can be useful for detecting low-mass ultra-short period planets (USP, defined with periods < 1 day). This has been discussed in Sulis et al. (2020). In addition to this very specific case, this section has two goals. The first goal is pedagogical as we illustrate the principle of the detection procedure with the simplest case. The second goal is to validate the proposed p -value estimation procedure when the NTS is composed with MHD simulations of stellar granulation and for irregular sampling. So far this validation has only been done for a regular sampling, in which case the FAP and p -values can be computed with analytical expressions (Sulis et al. 2020).

Fig. 2: Part of the 3SD procedure that estimates the p -value of Algorithm 1 (Algorithm 2).

4.2. Validation of the 3SD procedure on solar data

4.2.1. Data, MHD simulations and sampling grids

The validation of the procedure on real data poses two difficulties. First, establishing for ground truth reference for the p -value that would be obtained with a NTS composed of genuine stellar convection noise requires implementing the oracle procedure (see Sec. 3.1), which in turn requires a very large number of genuine stellar noise time series. Fortunately, the GOLF/SoHO spectrophotometer has made available 25-year-long time series

of solar RV observations that can be used (e.g., see Appourchaux et al. 2018). Second, as in this section we focus on granulation and instrumental noises only, we need to disregard the low frequency part of the noise PSD that is dominated by the magnetic activity. For that purpose, the detection test will be applied to frequencies $\nu > 56 \mu\text{Hz}$ only, since at frequencies below $56 \mu\text{Hz}$ the PSDs of solar data and MHD simulations start diverging (see Sulis et al. 2020 and Appendix C).

Since GOLF observations cover a very long period of time and since the granulation characteristic timescales are shorter

than a day, we divided the total time series into smaller series and focused only on this short-timescale solar variability. We selected $b = 1420$ two-day long series among the ≈ 3000 available time series taken during the first 17 years of GOLF observations (the last years are particularly affected by detector ageing).

These time series are regularly sampled ($N_{reg} = 2880$ data points) at sampling rate $\Delta t = 60$ s. As detailed in [Sulis et al. \(2020\)](#), we filtered out the high-frequency p-modes on each two-day-long series (with periods < 15 min, because they are not reproduced by the MHD simulations) and we added a WGN with variance σ_w^2 estimated from the high frequency plateau visible in the periodogram of the GOLF data (see Appendix C). The resulting data set constitutes a large set of noise time series from which the oracle's reference results can be computed.

Regarding the implementation of Algorithm 2, the available NTS is composed with a 53-day-long noise time series obtained from 3D MHD simulations of solar granulation (Bigot et al., in prep.). After splitting into two-day-long time series, 26 granulation noise time series are available, of which we randomly selected $L = 5$ for the standardization. Before running Algorithm 2, we applied to the NTS obtained from MHD simulations (\mathcal{T}_5) the same corrections as for the GOLF data (i.e., filtering of the stellar acoustic modes and addition of an instrumental WGN). The NTS was finally sampled as the observations under test (see the three sampling grids detailed just below).

Algorithm 2 also relies on parameters that set the size of the MC simulations, B and b (taken here respectively as $B = 100$ and $b = 10^4$) and on model \mathcal{M}_n with associated parameters $\hat{\theta}_n$. We choose here an AR model because it suits well to our MHD NTS time series and its parameters are fast to estimate. An AR process is defined as ([Brockwell & Davis 1991](#)):

$$\mathbf{n}(t_j) = \sum_{j=1}^{o_{AR}} \alpha_{AR,j} \mathbf{n}(t_j - j\Delta t) + \mathbf{w}(t_j), \quad j = 1, \dots, N \quad (8)$$

with $\mathbf{n}(t_j)$ the sample of \mathbf{n} at time instant t_j , $\alpha_{AR,j} \in]-1; 1[$ the AR coefficients filter, o_{AR} the AR order, Δt the sampling time step, and $\mathbf{w}(t_j)$ the sample at time t_j of a WGN series \mathbf{w} of variance σ_w^2 . The model parameters $\hat{\theta}_n$ are the AR order and the filter coefficients. The order is selected using Akaike's Final Prediction Error criterion ([Akaike 1969](#)) and leads to a value of 10, which remains fixed for the rest of the procedure. The filter coefficients (estimated $B \times b + 1$ times) are obtained through the standard Yule-Walker equations ([Brockwell & Davis 1991](#)).

For this study we consider three temporal sampling grids:

- a regular sampling grid ($\Delta t = 10$ minutes), where we keep only 10% of the initial GOLF series to make the number of data point N comparable to ordinary RV time series,
- a regular sampling grid ($\Delta t = 60$ seconds) affected by a large central gap: two times 2.4 h continuous observations separated by a 43.2 h gap.
- a random sampling grid, where 10% of data points are randomly selected in the initial regular grid of the GOLF series ($\Delta t \in [60, 2880]$ seconds).

In each case, the sampling grid contains $N = 288$ data points. For the regular (resp. irregular) sampling grids, the standardized periodogram is computed using the classical (resp. Lomb-Scargle) periodogram – both are the same for regular sampling.

4.2.2. Validation of Algorithm 2 on solar data

The p -value estimation procedure provided by Algorithm 2 results in $B = 100$ estimates $\hat{p}_v^{(i)}$ shown in grey in the top panels

of Fig. 3. The average p -value $\bar{\hat{p}}_v$, is shown in black and the p -value of the oracle procedure based on genuine stellar noise in green⁵. The beam of the grey curves represents particular estimates of the unknown relation $p_v(t)$ of the Algorithm 1, with parameters that are consistent with the NTS at hand. The true p -value of this procedure is unknown (in the irregular sampling case), because evaluating it exactly would require an infinite amount of MHD simulations. If the simulations done in Algorithm 2 sample well the space of parameters that are within error bars compatible with this NTS, the truth is likely to lie somewhere in these curves, perhaps close to the mean where the bunch of curves resides.

Comparing the black and green curves, we see that for the three considered sampling grids the approach based on MHD simulations is on average equivalent to using true stellar noise. This shows that while Algorithm 2 has only at hand a reduced number ($L = 5$) of synthetic time series for the NTS, it can generate a beam of situations whose mean succeeds in evaluating the true p -value of a standardized detection procedure supervised by genuine stellar noise.

We note a slight mismatch in the middle and right panel, probably because our ground truth (GOLF) data contain some effects that were not accounted for in the p -value estimation procedure. Here, the largest p -value (upper envelope of the grey curves) provides a more conservative and more reliable estimate than the mean. The test statistic t corresponding to a mean p -value of 1% are respectively (28.3, 33.6, 33.5) for the three samplings. For these values, the simulations show that the p -value have an empirical probability of 90% to lie in the range [0.4%, 1.6%], [0.5%, 1.5%], and [0.6%, 1.5%] respectively (panels in the middle row of Fig. 3). At these t values, the oracle p -values correspond to [1.2%, 1.8%, 1.3%], respectively.

Since MHD simulations are aimed at reproducing with great realism the stellar granulation noise, the good match observed in each case between the mean p -value obtained by Algorithm 2 and the oracle based on true stellar noise suggests that the true p -value is close to the sample average.

Note also that in the case of regular sampling, for which the p -value expression is known and given in Eq. (13) of [Sulis et al. \(2020\)](#), there is a good match between theory, the averaged estimate from Algorithm 2, and the oracle with true stellar noise (panel a).

Finally, the bottom panels show the histograms of the distribution of the frequency index where the maximum of the standardized periodogram was found during the iterations of Algorithm 2 of the 3SD procedure (grey) and oracle (green). In blue, we see the same distribution but for the (un-standardized) LSP i.e., a procedure that would apply the Max test to \mathbf{p} instead of $\bar{\mathbf{p}}$ in Algorithm 1. Because the noise is colored, we see that the LSP tends to peak at lower frequencies, where the PSD has larger values (see Fig. C.1). Colored noise inexorably causes an increased rate of false alarms at these frequencies but this effect cannot be quantified nor even suspected by the user when the noise PSD is unknown. In contrast, the standardization used in (5) leads to a more reasonable (uniform) distribution of the frequency index of the maximum peak. These results show that the 3SD pro-

⁵ For the oracle, Algorithm 1 was computed for the 1420 GOLF time series further permuted by blocks 10 times. This led to an effective number of $b = 14200$ series. To compute each realisation of the test we randomly selected one series to compute the periodogram in row 4 of Algorithm 1 and $L = 5$ other series to compute the averaged periodogram in row 14.

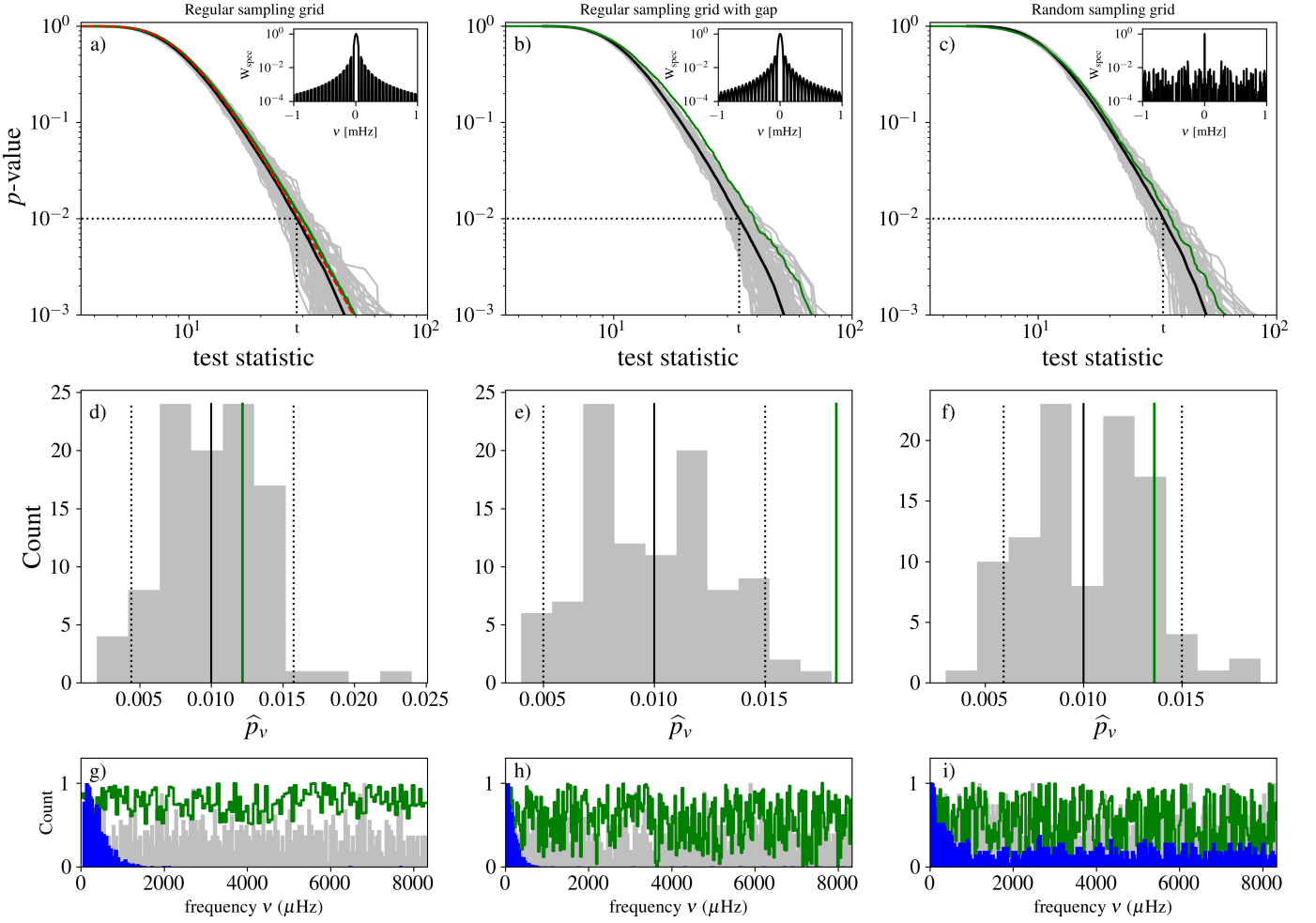


Fig. 3: Validation of the 3SD approach for a noise \mathbf{n} composed with granulation plus WGN and $\mathbf{d} = \mathbf{0}$ in (1). We investigate three temporal sampling grids, from left to right: regular, regular with a central gap, and random. **Top panels.** Green: Relation $p_v(t)$ for the detection procedure using a genuine NTS based on GOLF solar data (oracle). Grey: The $B = 100$ estimates $\hat{p}_v^{(i)}$ produced by the 3SD procedure using the MHD-based NTS. Black: Sample mean value $\bar{\hat{p}}_v$ of the grey curves. The spectral window of each sampling grid is shown in the inset panels. In panel a), the red line represents the analytical expression of the p_v (see Eq.(13) of Sulis et al. 2020). The dotted lines indicate the test statistic for which $\bar{\hat{p}}_v$ equals a mean p -value of 1%. **Middle panels.** Empirical distribution of the $\hat{p}_v^{(i)}$ at t and 90% intervals (dotted lines) around the mean (solid black lines). P -values obtained with the oracle are shown with the green vertical lines. **Bottom panels.** Grey: Example, for one of the B loops of Algorithm 2, of the empirical distribution of the $b = 10^4$ random values of the frequency index where the largest periodogram peak was found. Green: Empirical distribution of the Max test related to the oracle procedure (only contours are shown for visibility). Blue: same distribution but for an un-standardized LSP (i.e., the Max test is applied to \mathbf{p} instead of $\bar{\mathbf{p}} \mid \bar{\mathbf{p}}_L$).

cedure is well calibrated and Algorithm 2 succeeds in estimating correctly the resulting p -value. Since the distribution of the test statistic is very similar for data standardized with true noise and for data standardized by means of MHD noise time series, these results also demonstrate that the MHD simulations can efficiently be exploited in place of a genuine noise NTS for periodogram standardization.

Finally, we carried out a similar validation of the output p -values but for another couple (periodogram, test). We selected the GLS periodogram (Zechmeister & Kürster 2009) and the test statistic of the N_C^{th} maximum periodogram value defined as:

$$T_C(\bar{\mathbf{p}} \mid \bar{\mathbf{p}}_L) := \bar{p}_{(N-N_C+1)}, \quad (9)$$

with $N_C \in \mathbb{N}^+$ a parameter related to the number of periodic components, and $\bar{p}_{(k)}$ the k -th order statistic of $\bar{\mathbf{p}}$. We note that

test T_C may be more discriminative against the null than the Max test $\max_k \bar{p}(v_k) = \bar{p}_{(N)}$ in (6) for multiple periodic components, as discussed by Chiu (1989) and Shimshoni (1971). The p -values resulting from Algorithm 2 computed for $N_C = 10$ in (9) and for the random sampling grid defined in Sec. 4.2.1 are shown in Fig. 4. These results illustrate that the reliability of the procedure is not tied to the couple (LSP, Max test).

5. Noise = Magnetic activity + long term trends + granulation + WGN

5.1. Setting and objectives

In practice, many stellar activity processes affect the RV observations (Meunier 2021) and an NTS is not available for all of them.

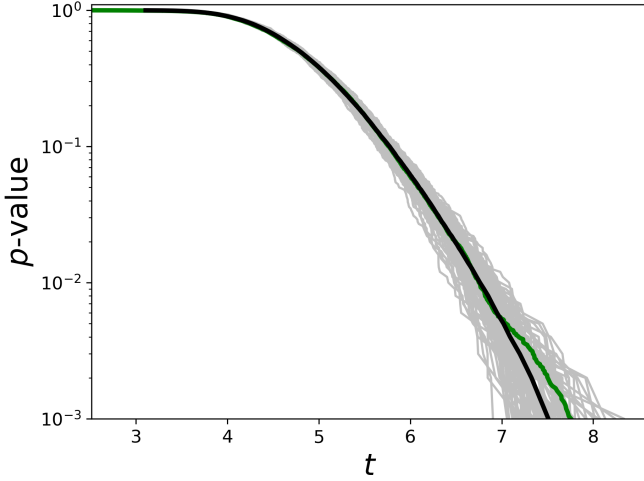


Fig. 4: Validation of Algorithm 2 using the GLS periodogram and test T_C in (9). Oracle is shown in green, p -value estimates from Algorithm 2 are shown in grey and their mean value in black.

This is the case, for example, of the stellar magnetic activity as starspots and plages. Here, we present a more general application of the 3SD procedure, where classical techniques used to correct for the stellar variability of magnetic sources are coupled with the use of an NTS. We will also investigate at the end of the section the case where no NTS is available.

In this section, we consider as an illustration a nuisance signal \mathbf{d} in (1) that encapsulates a magnetic signature modulated with the stellar rotation period plus long term trends modulated with the stellar cycle. Numerous techniques have been developed to estimate the contribution of magnetic activity to RV data (e.g., see Ahner et al. 2021). We assume that an estimate of the noise activity signature has been obtained by one of these methods, in the form of an ancillary time series for \mathbf{d} . This ancillary time series is assumed to be the log R'_{HK} activity indicator in the following (but other indicators could be used as well, see Table 1). The noise component \mathbf{n} in (1) is composed of correlated granulation noise plus WGN. An NTS of \mathbf{n} composed with L simulated RV time series obtained from MHD simulations is assumed available, except in the last part of this section where we relax this assumption.

The rest of this section contains four parts. The first two parts describe respectively the synthetic dataset with the computation of oracle p -values, and the validation of the p -value estimation algorithm with the impact of the priors on the computed p -values. In the third part, we study improvements that can be brought by using Generalized Extreme Values to speed up the Monte Carlo simulations in Algorithm 2. In the last part, we consider the particular (but practical) case where no NTS is available for \mathbf{n} in (1).

5.2. Synthetic RV time series and oracle p -values

We first create synthetic RV time series used to i) generate an RV test time series that will be used in the input of Algorithm 1, and ii) compute the oracle p -values that will be used to evaluate the accuracy of the p -value estimates derived from Algorithm 2. These time series entail magnetic, granulation and instrumental noises generated as follows.

Component \mathbf{d} is obtained as the realisation of a Gaussian process (GP, Rasmussen & Williams 2005) of kernel

$$k(t_i, t_j) = \alpha_{GP} k_E(t_i, t_j) + k_M(t_i, t_j), \quad (10)$$

with k_E and exponential sine square kernel defined as

$$k_E(t_i, t_j) = \exp \left\{ -\Gamma_{GP} \sin^2 \left(\pi |t_i - t_j| P_{GP}^{-1} \right) \right\}, \quad (11)$$

and k_M a Matérn-3/2 kernel defined as

$$k_M(t_i, t_j) = \left(1 + \sqrt{3} |t_i - t_j| \lambda_{GP}^{-1} \right) \exp \left\{ -\sqrt{3} |t_i - t_j| \lambda_{GP}^{-1} \right\}, \quad (12)$$

with $\{t_i, t_j\}$ the time coordinates at indexes $i, j = 1, \dots, N$. The hyper-parameters of kernel k in (10) are set to: $\alpha_{GP} = 2$, $\Gamma_{GP} = 22$ the scale parameter, $P_{GP} = 25$ days the rotation period, and $\lambda_{GP} = 1.609$ the characteristic length scale. The implementation of this GP is made using the GEORGE Python package⁶ (see Ambikasaran et al. (2015) and online documentation⁷ to find Eqs. (11) and (12)). Similar equations for kernels (11) and (12) can also be found in Eq.(8) of Espinoza et al. (2019) and Eq.(4) of Barragán et al. (2022) for instance.

This GP model with the same parameters is also used to compute the synthetic ancillary time series $\mathbf{c} := [c(t_1), \dots, c(t_N)]^T$, to which we add a WGN.

For component \mathbf{n} , we create a stochastic colored noise time series with an Harvey function and a WGN. The power spectral density of this noise model has the form (Harvey 1985, Meunier et al. 2015):

$$S_H(v_k^+; \theta_{\mathbf{n}}) := \left(\frac{\frac{2\sqrt{2}}{\pi} \frac{a_H^2}{b_H}}{1 + \left(\frac{v_k^+}{b_H} \right)^{c_H}} \right) + \sigma_{\mathbf{w}}^2, \quad (13)$$

where vector $\theta_{\mathbf{n}} := [a_H, b_H, c_H, \sigma_{\mathbf{w}}^2]^T$ collects the amplitude, characteristic frequency and power of the Harvey function, and $\sigma_{\mathbf{w}}^2$ is the variance of the WGN. Notation v_k^+ means that positive frequencies are considered. We calibrated the parameters vector $\theta_{\mathbf{n}}$ using a fit⁸ of the available MHD RV time series (see Sec. 4). Synthetic time series having PSD exactly given by (13) can be simulated with the Fourier Transform⁹.

An example of a synthetic 10-day-long time series obtained using models (10) and (13) is shown in Fig. 5 (black). From this time series, we created a large central gap between day 2 and day 8 in the time sampling grid, and we randomly selected $N = 288$ data points in the two remaining intervals (grey). This synthetic RV time series is the series under test in the three next subsections.

To compute the oracle procedure (which is a procedure that has knowledge of the exact parameters used to generate the synthetic time series, namely, $\theta_{\mathbf{n}}$ in (13) and $[\alpha_{GP}, \Gamma_{GP}, P_{GP}, \lambda_{GP}]$ in (10)), we generated 10^4 synthetic noise time series as described above and we ran Algorithm 1 for each of them. The resulting oracle ground truth is shown in green in Fig. 6 (all panels), Fig. 7 and Fig. 8.

⁶ <https://github.com/dfm/george>

⁷ <https://george.readthedocs.io/en/latest/user/kernels/>

⁸ In this case and in the following, we used the lmfit Python package (Newville et al. 2014), which makes non-linear optimizations for curve fitting problems. This choice was made for simplicity and because the algorithm is fast. For practical RV analyses, the user can optimize the fitting procedure, for e.g. using proper Markov Chain Monte Carlo estimation procedure.

⁹ To compute a synthetic time series from (13), we generate a WGN $\mathbf{w} \sim \mathcal{N}(\mathbf{0}, \mathbf{I})$, compute the FFT of \mathbf{w} , perform a pointwise multiplication with $\sqrt{S_H(v_k)}$ and take the real part of the inverse FT.

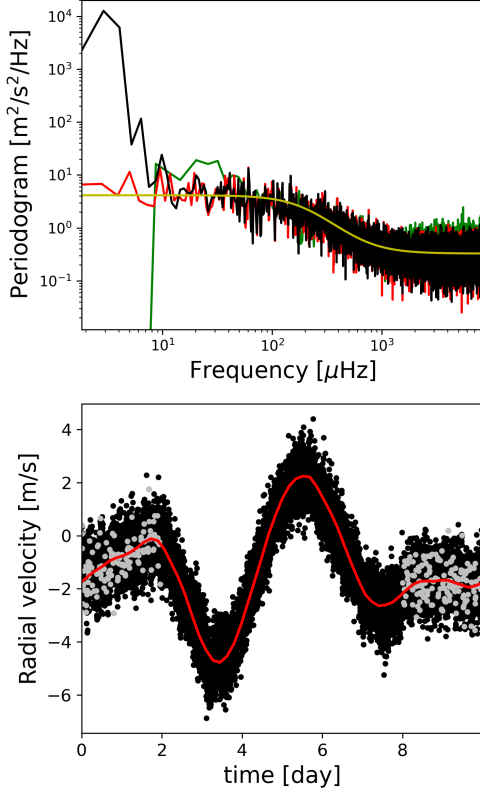


Fig. 5: Example of synthetic time series generated for the validation of the 3SD approach for the case noise = magnetic activity + long term trends + granulation + WGN. **Top**: averaged periodograms of the 2-days GOLF solar observations used in Sec. 2.4 (green) and the associated MHD training data (red), Harvey model fit to the MHD PSD (yellow), and averaged periodogram of the final synthetic data (GP+Harvey, black). **Bottom**: example of synthetic RV data generated with a regular sampling (black) based on a GP noise modeling for the magnetic activity (red). For the study, the dataset has further been irregularly sampled (grey).

5.3. Validation of Algorithm 2

We apply the 3SD procedure on one of the synthetic time series. For that purpose, we place ourselves in a realistic situation where the noise models \mathcal{M}_d and \mathcal{M}_n used as inputs of Algorithms 1 and 2 are different from the models used to generate the synthetic RV dataset in Sec. 5.2.

Following an example given in Dumusque et al. (2012) and Ahner et al. (2021), we use for \mathcal{M}_d a simple parametric model¹⁰ composed of a linear combination of \mathbf{c} and three low order polynomials :

$$\mathbf{d}(t_j | \boldsymbol{\theta}_d) = \beta_d \cdot \mathbf{c}(t_j) + \epsilon_d \cdot t_j^2 + \zeta_d \cdot t_j + \eta_d, \quad j = 1, \dots, N \quad (14)$$

with $\boldsymbol{\theta}_d = [\beta_d, \epsilon_d, \zeta_d, \eta_d]^\top$ the corresponding parameter vector.

For the available NTS \mathcal{T}_L , we select the $L = 5$ MHD time series described in Sec. 4.2.1. Using the LSP for \mathbf{P} , the Max test for \mathbf{T} , \mathcal{T}_L , the model (14) for \mathcal{M}_d , no model \mathcal{M}_n , and the synthetic ancillary series \mathbf{c} , we then compute Algorithm 1 and obtain a test value t .

¹⁰ This model is currently implemented in the code (see Appendix. A). Other models for \mathcal{M}_d , such as Gaussian process are not implemented yet, mainly for computational cost reasons.

To compute Algorithm 2, the inputs parameters (\mathbf{P} , \mathbf{T}), \mathcal{M}_d , and \mathbf{c} remain the same as for Algorithm 1. For the additional inputs, we take the result from row 2 of Algorithm 1 to obtain $\widehat{\boldsymbol{\theta}}_d$, the vector of (four) parameters estimates, along with its scale parameter $\widehat{\delta}_d$. We select a uniform prior π_d for the noise parameters with interval widths set to twice the estimated standard error. We select an AR model (8) for model \mathcal{M}_n (as in Sec. 4.1), and we fit this model to the NTS to obtain the estimated parameters $\widehat{\boldsymbol{\theta}}_n$. We finally set up the size of the MC simulations to $B = 100$ and $b = 1000$. The p -value estimates resulting from Algorithm 2 are shown in the left panel of Fig. 6. Comparing them with the oracle p -values, this shows that Algorithm 2 provides reliable p -value estimates at any t in the case of colored noise and activity.

As a final validation step of Algorithm 2, we finally examine the impact of the priors π_d (involved in row 13) on the derived p -values. Results are shown in Fig. 7. We observe in this example a weak impact, with accurate estimation for any t in almost all cases. If one goes as extreme as 10σ for the perturbation interval's width, we see that the p -value estimate becomes more conservative: at a given value of t the estimated p -value is biased upwards (blue curve). In practice, the influence of the chosen priors on the estimated p -values can always be checked by a simulation study of this kind.

5.4. Generalized Extreme Values

Algorithm 2 does not rely on any model for the estimated CDF $\widehat{\Phi}_{T|\mathcal{H}_0}$ of the test statistic (6). Hence, for the estimated mean p -value to be accurate, it requires the parameter b involved in Algorithm 2 to be large (typically $b \geq 1000$ or more). As $B \times b$ Monte Carlo simulations are involved (with B typically ≥ 100), Algorithm 2 is computationally expensive. Fortunately, univariate extreme-value theory shows that the maximum of a set of identically distributed random variables follows a Generalized Extreme Values (GEV) distribution (Coles 2001). This suggests that GEV distributions can be used as a parametric model for the CDF of (6) to improve the estimation accuracy. This method was used by Süveges (2014) for the case where only white noise is involved in model (1) (i.e., no colored noise nor nuisance signal \mathbf{d}). In Sulis et al. (2017b), we extended the work of Süveges (2014) to the case of a colored noise. Here, we evaluate the gains that can be brought by this parameterization into the bootstrap procedure for the general case of colored noise and magnetic activity signals.

The GEV's CDF depends on three parameters, the location $\mu \in \mathbb{R}$, the scale $\sigma \in \mathbb{R}^+$ and the shape $\xi \in \mathbb{R}$:

$$G(t) = e^{-\left[1 + \xi \left(\frac{t - \mu}{\sigma}\right)\right]_+^{-\frac{1}{\xi}}}, \quad (15)$$

with $[x]_+ := \max(0, x)$. In the case $\xi \neq 0$, $G(t)$ in (15) is only defined for $t = 1 + \xi \frac{t - \mu}{\sigma} > 0$. In the case $\xi = 0$, $G(t)$ is derived by taking the limit at $t = 0$.

In Algorithm 2, the unknown parameters $\boldsymbol{\theta}_{GEV} := [\xi, \mu, \sigma]^\top$ can be estimated using the $j = 1, \dots, b$ test statistics $t(\mathbf{x}^{(i,j)})$, for instance by maximum likelihood. In this case the maximization can be obtained by an iterative method (Coles 2001). This leads to $i = 1, \dots, B$ GEV parameters $\widehat{\boldsymbol{\theta}}_{GEV}^{(i)} := [\widehat{\xi}^{(i)}, \widehat{\mu}^{(i)}, \widehat{\sigma}^{(i)}]^\top$, from which the p -value can be estimated by $\widehat{p}_v^{(i)}(t) := 1 - G(t|\widehat{\boldsymbol{\theta}}_{GEV}^{(i)})$.

Results of the GEV parameterization are shown in the middle and right panels of Fig. 6 (for $b = 100$ and $b = 500$,

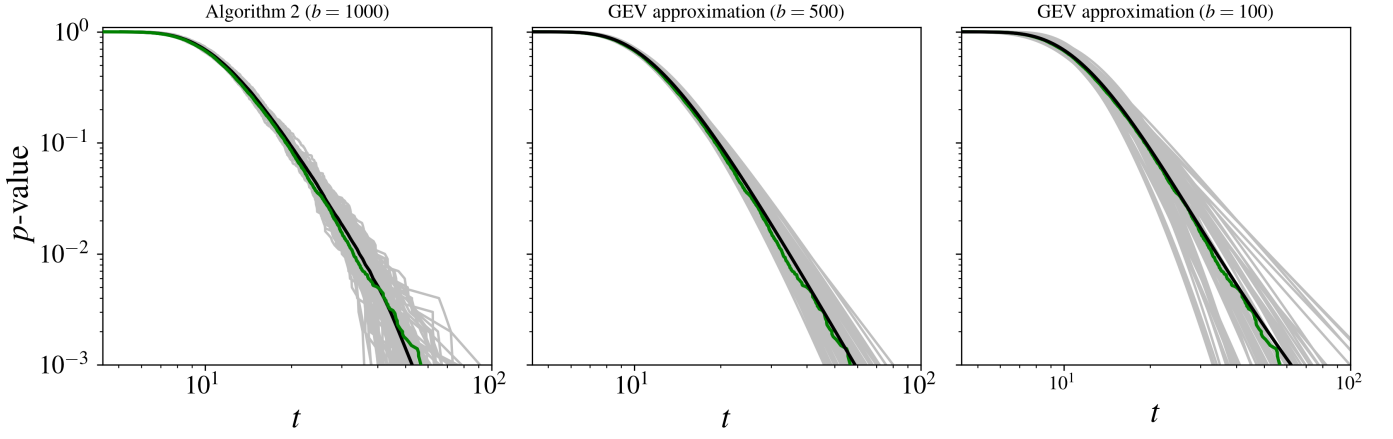


Fig. 6: p -value estimates resulting from Algorithm 1 for the case where noise = magnetic activity + long term trends + granulation + WGN, and where an NTS is available for granulation + WGN. The mean p -value is shown in black. The oracle, which is the same for all three panels, is shown in green. From left to right: Algorithm 2 computed without the GEV, and with the GEV approximation with $b = 500$ and $b = 100$, respectively.

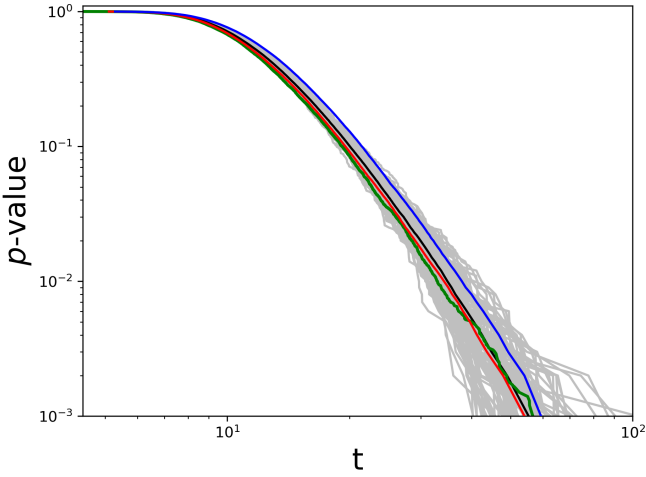


Fig. 7: p -value estimates resulting for different choice of priors $\pi_{\mathbf{d}}$ in row 13 of Algorithm 2. Grey and black: results for a Gaussian prior centered on the estimated parameters values with scale parameters taken as 3σ , with σ the estimated standard deviation of the parameters' estimates. Grey: examples of p -values $\hat{p}_v(t)$; black: mean p -value. Red and blue: results for uniform priors with intervals centered on the estimated parameters values and widths taken as 1σ (red) and 10σ (blue). The true (oracle) p -value is shown in green.

respectively). We see the p -value estimates resulting from the GEV approximation are still given in a fairly tight 90% interval around the oracle. We also see that, using only half of the MC realizations compared to the initial b value involved in Algorithm 2 ($b = 500$ instead of 1000), leads to a similar precision on the p -value estimates. Hence, the GEV approximation allows to halve the computational time of Algorithm 2 for the same precision (case $b = 500$). Reducing the computational time by ten ($b = 100$) leads to larger 90% intervals at constant p -value (e.g., we observe an interval $\sim 40\%$ larger at p -value of 1% in the right panel of Fig. 6).

5.5. Algorithm 2 with no NTS available (practical case)

We consider now the common situation where no NTS is available. In this case, the parameters of noise \mathbf{n} can be estimated from the data (possibly along with the magnetic activity signal \mathbf{d}), through a model $\mathcal{M}_{\mathbf{n}}$. Standardization is then performed by generating synthetic time series according to $\mathcal{M}_{\mathbf{n}}$ in Algorithm 1.

When no NTS is available, two steps in Algorithm 2 deserve a particular attention:

- First, in rows 3 and 4, we set $L = 1$ since the noise parameters estimate $\hat{\theta}_{\mathbf{n}}$ of model $\mathcal{M}_{\mathbf{n}}$ is based on the unique time series under test \mathbf{x} ,
- Second, in row 7, one can generate as many synthetic time series that follow model $\mathcal{M}_{\mathbf{n}}(\theta_{\mathbf{n}})$ as necessary. Hence, in principle, $L \rightarrow \infty$. In practice, however, the choice of L is a compromise between estimation error and computation time. For the purpose of making massive Monte Carlo simulations, we use in this study the small value $L = 5$.

As in Sec. 5.3, we apply the 3SD procedure to one of the synthetic time series described in Sec. 5.2.

We first run Algorithm 1 with model $\mathcal{M}_{\mathbf{d}}$ such that

$$\mathbf{d}(t_j | \theta_{\mathbf{d}}) = \beta_{\mathbf{d}} \cdot \mathbf{c}(t_j), \quad j = 1, \dots, N. \quad (16)$$

For model $\mathcal{M}_{\mathbf{n}}$, a Harvey function (13) is used. There is no NTS and the couple (P,T) is taken as the LSP periodogram and the Max test.

To compute Algorithm 2, the inputs parameters (P, T), $\mathcal{M}_{\mathbf{d}}$, $\mathcal{M}_{\mathbf{n}}$ and \mathbf{c} are the same as for Algorithm 1. For the additional inputs, we obtain $\hat{\theta}_{\mathbf{d}}$ and $\hat{\delta}_{\mathbf{d}}$ from row 2 of Algorithm 1 and set $\pi_{\mathbf{d}}$ as in Sec. 5.3. Parameters $\hat{\theta}_{\mathbf{n}}$ are obtained from row 9 of Algorithm 1, based on a fit of the LSP of \mathbf{x} (as in Dumusque et al. (2011)); this implicitly assumes that the LSP provides an acceptable approximation of the true PSD). We finally set up the size of the MC simulations to $B = 100$ and $b = 1000$. The p -value estimates resulting from Algorithm 2 are shown in Fig. 8. We observe a very good match between the estimated mean p -values and true p -values, similarly to the case with an NTS (Sec. 5.3, see left panel of Fig. 6). This shows that the p -value can be robustly estimated even in the case where no NTS is available.

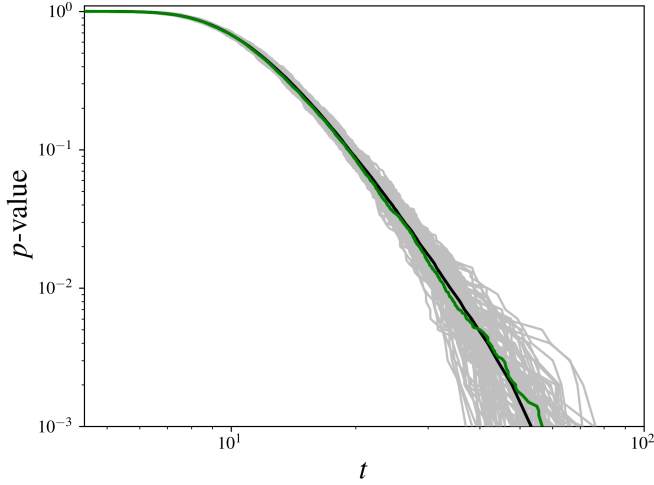


Fig. 8: Same as Fig. 6 but for a practical case where no NTS is available for \mathbf{n} in (1). In this case, the covariance structure of the stochastic noise source is estimated from the data with model $\mathcal{M}_{\mathbf{n}}$ given in (13).

We anticipate, however, that the performances of detection procedures based on estimates of the covariance structure from the data will probably depend on the RV data (noise sources, data sampling,...). The comparison of specific cases is left to a future paper.

6. Application to RV exoplanet detection: the case of the debated detection α CenBb

Alpha Centauri Bb is a debated ~ 1.13 Earth mass (minimum mass) planet whose detection was reported around our solar neighborhood star α CenB with an orbital period of 3.2 days (Dumusque et al. 2012). Achieving the detection of such a small planet is a challenge as α Cen is a triple star and the planetary RV semi-amplitude (~ 0.51 m/s) was at the limit of the instrumental precision of HARPS (~ 1 m/s). The observed RV campaign contains $N = 459$ points, irregularly sampled during a time span of 4 years between 2008 and 2011. The dataset contains big gaps between the years of observations due to the star visibility and small gaps due to the available nights.

The planet detection has been largely debated: using analysis tools different from the detection paper in Hatzes (2013), using a different stellar noise modeling in Rajpaul et al. (2016) and recently using a different technique of randomization inference to measure the p -value of the periodogram peak at 3.2 days by Toulis & Bean (2021).

In this section, we analyse this RV dataset as a case-study for the 3SD procedure. The objective of the second part (Sec. 6.2) is also to demonstrate that Algorithm 2 offers the possibility to investigate the effects of model errors on the frequency analysis and on the estimated p -values. The purpose is not to argue for or against a chosen noise model but to study the effects of model mismatch. We first present the results of the 3SD procedure computed with the noise models involved in the detection paper (Dumusque et al. 2012). We then analyze the robustness of the results using a different noise model.

6.1. 3SD procedure with models from the detection paper

In short, the initial model $\mathcal{M}_{\mathbf{d}}$ described in the detection paper (Dumusque et al. 2012) contains three noise components:

- the binary contribution (\mathbf{m}_B) of α Cen A, modeled with a second order polynomial (3 free parameters).
- the magnetic cycle, modeled with the linear relation (16) and the $\log R'_{\text{HK}}$ (for which periods < 40 days have been filtered out) taken as ancillary series (\mathbf{m}_C , 1 free parameter).
- the magnetic (rotation modulated) activity (\mathbf{m}_M), modeled as the sum of sines and cosines waves fitted at the stellar rotation period (~ 37 days) and its four first harmonics. Due to the stellar differential rotation, the authors fitted each four years of observations individually to allow the stellar rotation period estimate to slightly vary from year to year. They also used a different number of harmonics for each four RV subsets¹¹. In total, \mathbf{m}_M contains 19 free parameters.

The sum of components \mathbf{m}_B , \mathbf{m}_C and \mathbf{m}_M forms the noise component \mathbf{d} in model (1). The authors assumed that component \mathbf{n} in (1) is uncorrelated and there is no NTS.

We applied the 3SD procedure to the RV data of α CenB with the following setting for Algorithm 1:

- the Lomb-Scargle periodogram as \mathcal{P} ,
- the Max test as \mathcal{T} ,
- the set of linearly sampled frequencies as $\Omega := [9.4 \times 10^{-4}, 215.8] \mu\text{Hz}$ (with $\Delta\nu = 1.88 \times 10^{-3} \mu\text{Hz}$, and $N_{\Omega} = 114750$ frequencies in total),
- no training time series or parametric model for the stochastic noise component \mathbf{n} ($\mathcal{T}_L = \emptyset$; $\mathcal{M}_{\mathbf{n}} = \emptyset$),
- the model defined in Dumusque et al. (2012) for component \mathbf{d} , recalled above as $\mathcal{M}_{\mathbf{d}}$,
- the ancillary time series \mathbf{c} as the 40-days filtered $\log R'_{\text{HK}}$ time series available from Dumusque et al. (2012)’s data release.

In row 11 of Algorithm 1, we obtained a standard deviation $\hat{\sigma}_{\mathbf{w}}$ of the data residuals of 1.23 m/s ¹², in agreement with the value given in Dumusque et al. (2012). The standardized periodogram computed in row 14 is shown in Fig. 9. The algorithm computed a test value $t = 16.03$ (peak at 3.2 days).

We then ran Algorithm 2 to evaluate the p -value of t with same inputs as Algorithm 1 that are listed above and:

- the number of MC simulations: $B = 100$ and $b = 1000$,
- a Gaussian prior for $\pi_{\mathbf{w}}$ with standard deviation 0.04 m/s (1σ estimated error bar),
- a uniform prior $\pi_{\mathbf{d}}$ with a 1σ interval width on each of the 23 free parameters of model $\mathcal{M}_{\mathbf{d}}$.

The t values corresponding to mean p -values of 10, 1 and 0.1% are shown respectively by solid green, blue and red curves in Fig. 9. The 90% intervals are shown with the corresponding colored shaded regions. The value $t := \tilde{\mathbf{p}}(3.2 \text{ d}) = 16.03$ corresponds to an estimated mean p -value of 0.47% with a 90% interval of [0.1%, 0.7%]. We checked that these results are reasonably stable with respect to the prior model $\pi_{\mathbf{d}}$ for the $\mathcal{M}_{\mathbf{d}}$ model parameters in row 13 of Algorithm 2 (e.g., a Gaussian instead of

¹¹ To save space in the present paper, we refer the reader to the ‘‘Supplementary material’’ of Dumusque et al. (2012) for the global model that is fitted to each four RV subset (see their Eqs. p.7).

¹² For these data different error bars estimates $\hat{\sigma}_i$ are provided and were considered in the parameters’ estimation. For simplicity, Algorithm 2 used a common uniform prior with interval equal to $\hat{\sigma}_{\mathbf{w}}$ but independent priors matched to the $\hat{\sigma}_i$ could be implemented here.

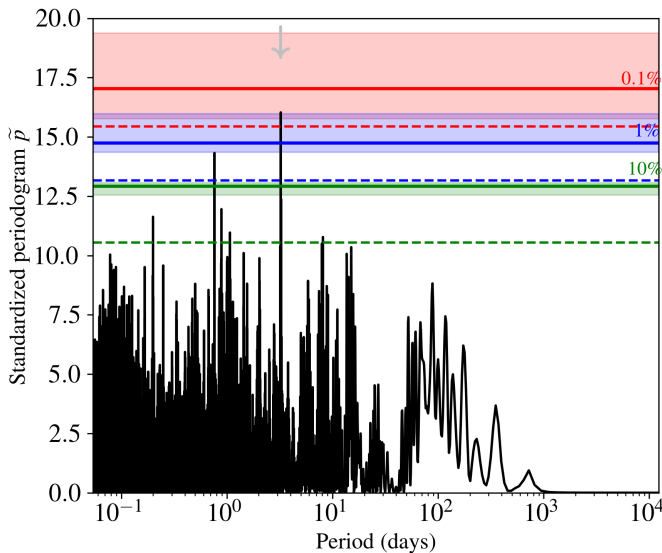


Fig. 9: Standardized Lomb-Scargle periodogram of the α Cen B RV residuals. The noise model \mathcal{M}_d used to create these residuals has been taken from Dumusque et al. (2012). p -values estimated by a classical bootstrap procedure (see text) are shown with the dashed lines. Mean p -values derived with Algorithm 2 are shown with the solid lines, and their credible interval with the shaded regions. The peak at 3.2 days is shown by the grey vertical arrow.

uniform prior with interval widths set to 1σ standard error leads to $\bar{p}_e(16.03) = 0.43\%$ with $[0.1\%, 0.7\%]$ 90% interval).

The study of Dumusque et al. (2012) made the assumption that the data residuals (without planet) are white. While the p -value evaluation procedure used in this paper was not specified, we assume they used the classical bootstrap technique where the p -values are evaluated by shuffling the dataset keeping the observing time dates constant. The t values corresponding to the p -values of 10, 1 and 0.1% computed with this classical method are shown by dashed lines for comparison. The largest periodogram peak at 3.2 days lies in the region of p -values below 0.1%, which is consistent with the result of the publication paper (a p -value of 0.02%).

We conclude from this analysis that if the model assumed by Dumusque et al. (2012) is accurate, the 3.2 days peak is associated with a mean p -value of 0.47%, which is small but nevertheless about 23 times larger than the 0.02% p -value estimate given in the detection paper. In general, the p -value derived without taking into account the errors on the noise model’s parameters are under-estimated.

6.2. Systematic study of noise model errors

We consider now another noise model \mathcal{M}_d for **d**. Following Rajpaul et al. (2016) (see their Sec. 4), we still consider a nuisance signal of the form $\mathbf{d} = \mathbf{m}_B + \mathbf{m}_C + \mathbf{m}_M$, but with some modifications. The estimation of the noise model’s parameters on the RV dataset is now performed in two steps. The binary and long-term trends components \mathbf{m}_B and \mathbf{m}_C are fitted first. The magnetic activity component \mathbf{m}_M is fitted in a second step on the data residuals as a Gaussian process with a quasi-periodic covariance kernel of the form of (10), with k_M fixed to 0 and parameters $[\alpha_{GP}, \Gamma_{GP}, P_{GP}]$ free with P_{GP} in interval $[30, 42]$ days.

If we run our detection Algorithm 1 with this new noise model, we get a final data residuals of 0.78 m/s standard deviation and the peak at 3.2 days disappears. Similarly to Rajpaul et al. (2016), we performed an “injection test” with planetary signal at 3.2 days of 0.51 m/s amplitude to verify that the GP noise model does not overfit the planet signal. We found the periodogram peak of the data residuals to be the highest peak, confirming the observations of Rajpaul et al. (2016) that the detection outcome can be very sensitive to the choice of the noise model plugged in the detection algorithm.

Model errors are unavoidable in practice. For the same dataset, different experts may assume different noise models and the magnitude of the absolute error committed by these models can probably be lower bounded by the relative difference between the models. These observations suggest that automatic studies of the robustness of the detection process to model errors should be incorporated in the process of estimating p -values. For this purpose, a “hybrid” version of the 3SD procedure can be used.

This hybrid version simply consists in two modifications of the 3SD procedure. First, we allow in Algorithm 2 the procedure to generate the noise training series in rows 12 to 15 with a given model \mathcal{M}_d (the Gaussian process model), and to fit it in row 16 with another model, say \mathcal{M}'_d (the Dumusque et al. (2012)’s model). Second, we do not use the standardization step in Algorithm 1 (rows 5 to 13), because data residuals resulting from different models will have different dispersions, with a larger dispersion in presence of model error. Keeping standardization (namely, division by the estimated variance) would then lead to relatively smaller $\bar{\mathbf{p}} | \bar{\mathbf{p}}_L$ components for the model with the largest residuals and artificially hide the effects of the mismatch we seek to evidence. The test values corresponding to p -values of 10, 1 and 0.1% computed in this hybrid configuration are shown with the horizontal dotted lines in Fig. 10 (left panel). For comparison, the levels corresponding to the no model error configuration are shown by solid lines. The 90% intervals are again shown with shaded regions. We find that if the detection process indeed used the right noise model, the largest data peak at 3.2 days has a p -value of 0.62%. If, however, the detection process committed a slight mismatch in the model error, the actual p -value of the same peak increases to 62.02%. This means that peaks as large as the largest data peaks happen actually quite often, even without planet, when the detection process is run under a model mismatch such as the one simulated here. Model mismatch is a likely situation in practice. A robust detection would be a detection whose p -value remains low under realistic model mismatches.

Interestingly, the hybrid version of the 3SD procedure further allows for investigation of the distribution of the period index where the $B \times b$ maximum values of \mathbf{p} are found (see in Sec. 4). This allows pointing towards periodicities that are not caused by planets and may be used as a warning in the detection process when it finds a planet at these frequencies. This distribution is shown in Fig. 10 (bottom right panel). In this case, the distribution of the frequency index of the largest periodogram peaks significantly moves away from the uniform distribution that is seen when the noise model is correct (top right panel). When the noise model is correct, each frequency has been randomly hit a few times (the holes are caused by frequencies killed in the noise model). In contrast, when the noise model is not correct, the maximum peak was found 2504 times at the 3.2 days period (against 2 times under no model error), or 1917 times at the 7.94 days period (against 1 time with no model error).

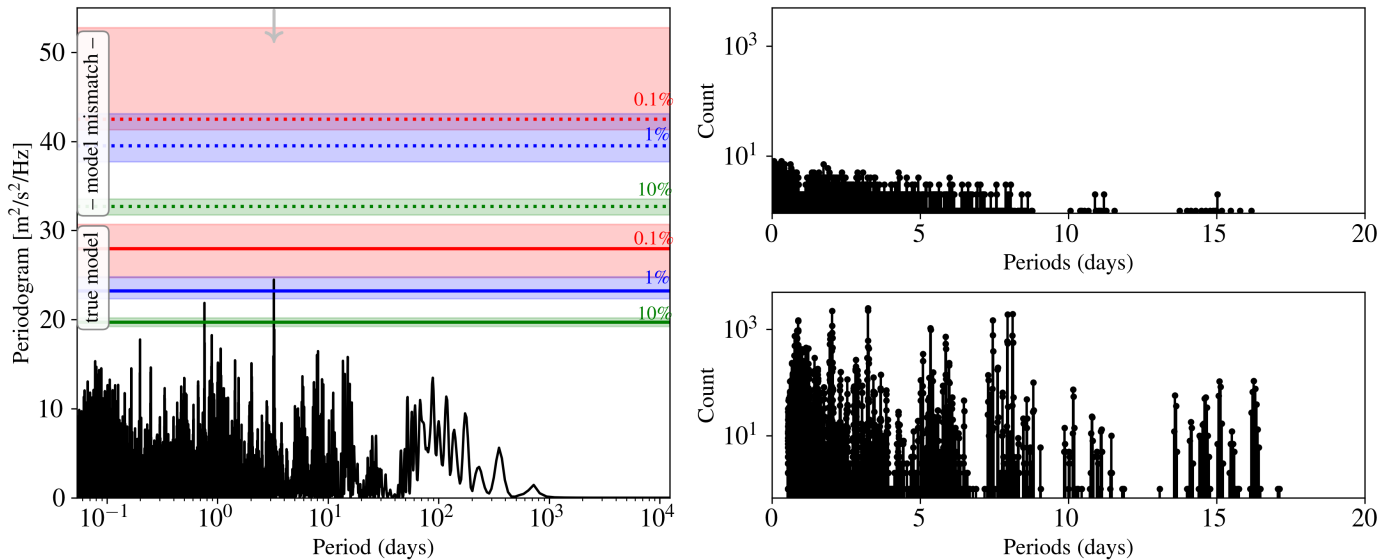


Fig. 10: Left: Lomb-Scargle periodogram of the α CenB RV residuals. The peak at 3.2 days is shown by the grey vertical arrow. Solid lines are the mean p -values estimated with no model error. The p -value at $t := \mathbf{p}(3.2 \text{ d}) = 24.48$ is in the 90% interval [0.1%, 0.7%]. Dotted lines are the mean p -values estimated with model error (see text). The p -value at $t = 24.48$ is this time in the 90% interval [59.5%, 64.7%]. Right: Distribution of the period index where the maximum periodogram value was found in row 15 of Algorithm 2 (zoom at periods < 20 days). The standard version of the 3SD procedure (simulating the situation without model error) is shown on the top panel and the hybrid version (detection process run with a model error) is shown in the bottom panel. We see a bias towards specific periods in the bottom panel: model error leaves residuals in which periodicities are imprinted.

In conclusion, when one 1) takes into account the estimation errors on the noise parameters (assuming no model error) and 2) investigates the effects of possible, realistic errors on the noise model, the “degree of surprise” brought by the peak at 3.2 days decreases substantially. This study of the α CenB dataset supports the same conclusion as previous works (Hatzes 2013, Rajpaul et al. 2016, Toulis & Bean 2021), namely a likely false detection at 3.2 days, but with a different analysis. Beyond the particular case of α CenB data set, accounting for possible noise model errors appears as a critical point, particularly when the amplitude of the planet signal is small compared to the nuisance signals.

7. Discussion and Conclusions

Assessing the significance level of detection tests is critical for exoplanet RV detection in the regime of low signal-on-noise ratio and in presence of colored noise of unknown statistics. Impacts of errors on parameters estimation and of model errors on p -values have deserved little attention in the exoplanet community so far.

To overcome this limitation, we have presented a new methodology to compute p -values of detection tests for RV planets detection in presence of unknown colored noise. The developed Bayesian procedure is based on the principles of statistical standardization and allows to use some “training samples” (NTS) if available (Sec. 2). It involves Monte Carlo simulations (Sec. 3) and allows to evaluate the robustness of the derived significance levels against specific model errors (Sec. 6.2). Our procedure builds on and extends our previous study Sulis et al. (2020), which was limited to the case of regular sampling and was not able to handle magnetic activity signals. This procedure allows to derive in Algorithm 2 the p -value corresponding to a test statistic produced in the detection Algorithm 1, while accounting for uncertainties in the noise model’s parameters.

Periodogram standardization can be implemented using a (possibly simulated) NTS. Examples of simulated NTS can come from MHD simulations of granulation, supergranulation or any other stellar simulations that are shown to be reliable. This opens future collaborations between stellar modelers and RV exoplanet scientists (see Sec. 4). The NTS can also come from instrumental measurements, independent of the studied RV dataset. In addition, the procedure can take advantage of ancillary data to deal with nuisance signals such as the stellar magnetic activity (e.g. $\log R'_{\text{HK}}$ time series).

Overall, the proposed detection procedure is versatile in

- the periodograms (or other frequency analysis tools),
- the detection tests (classical or adaptive),
- the noise models

that can be plugged-in. Examples of input parameters for the three items above are listed in Table 1. Additionally, Python codes are released on GitHub (see Appendix. A). Although not emphasized in this paper, the 3SD procedure also opens the possibility of using adaptive tests as the Higher Criticism or the Berk-Jones tests (Donoho & Jin 2004, Berk & Jones 1979). These tests are more powerful than classical detection tests (as the Max test presented in (6)) in the case of “exotic” planet signatures of small amplitudes (e.g., planets of high eccentricity, multi-planet systems) when the data sampling is regular (see Sulis et al. 2017a). Incorporating these adaptive tests in the proposed 3SD procedure to evaluate their performance in the context of irregular time sampling will be investigated in a further study.

In the paper, we have illustrated how the procedure can be implemented in the presence of instrumental, granulation, magnetic activity, long term drifts of stellar origin (magnetic cycle), and binary noises in model (1) (Sec. 4, 5, 6). Other RV noise sources can similarly be considered in the procedure when identified in the RV data.

Implementing the 3SD procedure may present some issues, but these can be – at least partially – solved.

- The procedure can be very time consuming owing to several factors (generation of NTS simulations, large number of MC simulations, complexity scaling with the number of parameters of the noise models). We have shown that the GEV framework allows us to reduce this computational cost (Sec. 5.4).
- The computed p -values remain dependent on the choice of the input noise models. While this is not specific to our approach, we showed that a “hybrid” version of the procedure allows us to quantify the robustness of p -value estimates to specific model changes (Sec. 6.2).
- The computed p -values are more conservative than the p -values obtained by random shuffling of the best fit residuals, as often done in RV data analysis (Sec. 6.1). This is because they take into account the main errors generated during the detection process (estimation error on the parameters and/or specific model error).
- When the detection process makes some error in the assumed noise model, estimating and removing a nuisance signal from the RV dataset may lead to a non uniform distribution of the frequency index where the largest periodogram peak is found (this is visible in the bottom right panel of Fig. 10). The reason is that imperfect subtraction of nuisance signals (caused by a model error) leads to residual long period signals in which the periodicities of the sampling grid are imprinted. Models error always remain in practice and the proposed algorithm allows to diagnose the effects of some of them.

Finally, throughout this paper, we have illustrated the proposed methodology on solar data, synthetic datasets as well as HARPS data of α CenB. The next step is to analyze some yet-to-be confirmed low-amplitude planets detection.

Acknowledgements. The authors would like to thank the referee for her/his helpful comments, which led to improved versions of this study. S. Sulis acknowledges support from CNES. D. Mary acknowledges support from the GDR ISIS through the *Projet exploratoire TASTY*. MHD stellar computations have been done on the “Mesocentre SIGAMM” machine, hosted by *Observatoire de la Côte d’Azur*. The GOLF instrument onboard SOHO is a cooperative effort of scientists, engineers, and technicians, to whom we are indebted. SOHO is a project of international collaboration between ESA and NASA. We acknowledge X. Dumusque, Astronomy Department Geneva Univ., Switzerland, for the public HARPS-N data that have been made available at <http://cdsarc.u-strasbg.fr/viz-bin/cat/J/A+A/648/A103>. We acknowledge support from PNP and PNPS-CNES for financial support through the project *ACTIVITE*.

References

- Ahrer, E., Queloz, D., Rajpaul, V. M., et al. 2021, *MNRAS*, 503, 1248
- Aigrain, S., Pont, F., & Zucker, S. 2012, *MNRAS*, 419, 3147
- Akaike, H. 1969, *Annals of the Institute of Statistical Mathematics*, 21, 243
- Ambikasaran, S., Foreman-Mackey, D., Greengard, L., Hogg, D. W., & O’Neil, M. 2015, *IEEE Transactions on Pattern Analysis and Machine Intelligence*, 38, 252
- Anglada-Escude, G., Arriagada, P., Tuomi, M., et al. 2014, *MNRAS*, 443, L89
- Appourchaux, T., Boumier, P., Leibacher, J. W., & Corbard, T. 2018, *A&A*, 617, A108
- Baluev, R. V. 2008, *MNRAS*, 385, 1279
- Baluev, R. V. 2011, *Celestial Mechanics and Dynamical Astronomy*, 111, 235
- Baluev, R. V. 2013a, *Astronomy and Computing*, 2, 18
- Baluev, R. V. 2013b, *MNRAS*, 429, 2052
- Baluev, R. V. 2015, *MNRAS*, 446, 1493
- Barragán, O., Aigrain, S., Rajpaul, V. M., & Zicher, N. 2022, *MNRAS*, 509, 866
- Bayarri, M. J. & Berger, J. O. 2000, *Journal of the American Statistical Association*, 95, 1127
- Berk, R. & Jones, D. 1979, *Z. Wahrscheinlichkeit.*, 47, 47
- Boisse, I., Bouchy, F., Hébrard, G., et al. 2011, *A&A*, 528, A4
- Bortle, A., Faussey, H., Ji, J., et al. 2021, *AJ*, 161, 230
- Bourguignon, S., Carfantan, H., & Böhm, T. 2007, *A&A*, 462, 379
- Box, G. E. P. 1980, *Journal of the Royal Statistical Society. Series A (General)*, 143, 383
- Brockwell, P. & Davis, R. 1991, *Time series : theory and methods* (Springer)
- Carleo, I., Malavolta, L., Lanza, A. F., et al. 2020, *A&A*, 638, A5
- Chiu, S.-T. 1989, *Journal of the Royal Statistical Society: Series B (Methodological)*, 51, 249
- Coles, S. G. 2001, *An Introduction to Statistical Modelling of Extreme Values* (Springer-Verlag, London)
- Collier Cameron, A., Ford, E. B., Shahaf, S., et al. 2021, *MNRAS*, 505, 1699
- Collier Cameron, A., Mortier, A., Phillips, D., et al. 2019, *MNRAS*, 487, 1082
- Cretignier, M., Dumusque, X., Hara, N. C., & Pepe, F. 2021, *A&A*, 653, A43
- Cumming, A. 2004, *MNRAS*, 354, 1165
- Cumming, A., Marcy, G. W., & Butler, R. P. 1999, *ApJ*, 526, 890
- Cunha, D., Santos, N. C., Figueira, P., et al. 2014, *A&A*, 568, A35
- Davis, A. B., Cisewski, J., Dumusque, X., Fischer, D. A., & Ford, E. B. 2017, *ApJ*, 846, 59
- de Beurs, Z. L., Vanderburg, A., Shallue, C. J., et al. 2020, *arXiv e-prints*, arXiv:2011.00003
- Delisle, J. B., Hara, N., & Ségransan, D. 2020, *A&A*, 635, A83
- Donoho, D. & Jin, J. 2004, *The Annals of Statistics*, 32, 962
- Donoho, D. L. & Johnstone, I. M. 1994, *Biometrika*, 81, 425
- Dumusque, X. 2018, *A&A*, 620, A47
- Dumusque, X., Cretignier, M., Sosnowska, D., et al. 2021, *A&A*, 648, A103
- Dumusque, X., Pepe, F., Lovis, C., et al. 2012, *Nature*, 491, 207
- Dumusque, X., Udry, S., Lovis, C., Santos, N. C., & Monteiro, M. J. P. F. G. 2011, *A&A*, 525, A140
- Efron, B. & Hastie, T. 2016, *Computer Age Statistical Inference: Algorithms, Evidence, and Data Science*, Institute of Mathematical Statistics Monographs (Cambridge University Press)
- Elorrieta, F., Eyheramendy, S., & Palma, W. 2019, *A&A*, 627, A120
- Espinoza, N., Kossakowski, D., & Brahm, R. 2019, *MNRAS*, 490, 2262
- Ferraz-Mello, S. 1981, *AJ*, 86, 619
- Fischer, D. A., Anglada-Escude, G., Arriagada, P., et al. 2016, *PASP*, 128, 066001
- Gregory, P. C. 2016, *MNRAS*, 458, 2604
- Guttman, I. 1967, *Journal of the Royal Statistical Society: Series B (Methodological)*, 29, 83
- Hanasoge, S. M., Duvall, T. L., & Sreenivasan, K. R. 2012, *Proceedings of the National Academy of Science*, 109, 11928
- Hara, N. C., Boué, G., Laskar, J., & Correia, A. C. M. 2017, *MNRAS*, 464, 1220
- Hara, N. C., Delisle, J.-B., Unger, N., & Dumusque, X. 2022, *A&A*, 658, A177
- Harvey, J. 1985, in *ESA Special Publication, Vol. 235, Future Missions in Solar, Heliospheric & Space Plasma Physics*, ed. E. Rolfe & B. Battrock, 199
- Hatzes, A. P. 2013, *ApJ*, 770, 133
- Hatzes, A. P., Cochran, W. D., Endl, M., et al. 2015, *A&A*, 580, A31
- Hatzes, A. P., Fridlund, M., Nachmani, G., et al. 2011, *ApJ*, 743, 75
- Horne, J. H. & Baliunas, S. L. 1986, *ApJ*, 302, 757
- Jenkins, J. S. & Tuomi, M. 2014, *ApJ*, 794, 110
- Jenkins, J. S., Yoma, N. B., Rojo, P., Mahu, R., & Wuth, J. 2014, *MNRAS*, 441, 2253
- Jones, D. E., Stenning, D. C., Ford, E. B., et al. 2022, *The Annals of Applied Statistics*, 16, 652
- Jurgenson, C. et al. 2016, in *Proc. SPIE, Vol. 9908, Ground-based and Airborne Instrumentation for Astronomy VI*, 99086T
- Kay, S. M. 1998, *Fundamentals of Statistical Signal Processing: Detection Theory*, 1st edn., Vol. 2 (Prentice-Hall PTR)
- Mary, D. & Roquain, E. 2021, *arXiv e-prints*, arXiv:2106.13501
- Ment, K., Fischer, D. A., Bakos, G., Howard, A. W., & Isaacson, H. 2018, *AJ*, 156, 213
- Meunier, N. 2021, in *Proceedings of the Evry Schatzman School 2019 "Interactions star-planet"*, ed. L. Bigot, J. Bouvier, Y. Lebreton, & A. Chiavassa
- Meunier, N. & Lagrange, A. M. 2019, *A&A*, 625, L6
- Meunier, N. & Lagrange, A. M. 2020, *A&A*, 638, A54
- Meunier, N., Lagrange, A. M., & Borgniet, S. 2017, *A&A*, 607, A6
- Meunier, N., Lagrange, A. M., Borgniet, S., & Rieutord, M. 2015, *A&A*, 583, A118
- Newville, M., Stensitzki, T., Allen, D. B., & Ingargiola, A. 2014, *LMFIT: Non-Linear Least-Square Minimization and Curve-Fitting for Python*
- Noyes, R. W., Hartmann, L. W., Baliunas, S. L., Duncan, D. K., & Vaughan, A. H. 1984, *ApJ*, 279, 763
- Paltani, S. 2004, *A&A*, 420, 789
- Palumbo, Michael L., I., Ford, E. B., Wright, J. T., et al. 2022, *ApJ*, 163, 11
- Pepe, F. A. et al. 2010, in *Proc. SPIE, Vol. 7735, Ground-based and Airborne Instrumentation for Astronomy III*
- Queloz, D., Henry, G. W., Sivan, J. P., et al. 2001, *A&A*, 379, 279
- Rajpaul, V., Aigrain, S., Osborne, M. A., Reece, S., & Roberts, S. 2015, *MNRAS*, 452, 2269
- Rajpaul, V., Aigrain, S., & Roberts, S. 2016, *MNRAS*, 456, L6

- Rajpaul, V. M., Buchhave, L. A., Lacedelli, G., et al. 2021, *MNRAS*, 507, 1847
- Rasmussen, C. E. & Williams, C. K. I. 2005, *Gaussian Processes for Machine Learning (Adaptive Computation and Machine Learning)* (The MIT Press)
- Reegen, P. 2007, *A&A*, 467, 1353
- Reichert, K., Reffert, S., Stock, S., Trifonov, T., & Quirrenbach, A. 2019, *A&A*, 625, A22
- Rincon, F. & Rieutord, M. 2018, *Living Reviews in Solar Physics*, 15, 6
- Roquain, E. & Verzelen, N. 2022, *The Annals of Statistics*, 50, 1095
- Rubin, D. B. 1984, *The Annals of Statistics*, 1151
- Santos, N. C., Mortier, A., Faria, J. P., et al. 2014, *A&A*, 566, A35
- Scargle, J. D. 1982, *ApJ*, 263, 835
- Schwarzenberg-Czerny, A. 1998, *MNRAS*, 301, 831
- Schwarzenberg-Czerny, A. 2012, in *New Horizons in Time Domain Astronomy*, ed. E. Griffin, R. Hanisch, & R. Seaman, Vol. 285, 81–86
- Seifahrt, A., Käufel, H. U., Zängl, G., et al. 2010, *A&A*, 524, A11
- Shimshoni, M. 1971, *Geophysical Journal*, 23, 373
- Sulis, S. 2017, *Theses, Université Côte d'Azur*
- Sulis, S., Mary, D., & Bigot, L. 2016, *IEEE International Conference on Acoustics, Speech and Signal Processing (ICASSP)*, Shanghai, 4428
- Sulis, S., Mary, D., & Bigot, L. 2017a, *IEEE TSP*, 65, 2136
- Sulis, S., Mary, D., & Bigot, L. 2017b, in *2017 25th European Signal Processing Conference (EUSIPCO)*, 1095–1099
- Sulis, S., Mary, D., & Bigot, L. 2020, *A&A*, 635, A146
- Süveges, M. 2014, *MNRAS*, 440, 2099
- Süveges, M., Guy, L. P., Eyer, L., et al. 2015, *MNRAS*, 450, 2052
- Tal-Or, L., Zechmeister, M., Reiners, A., et al. 2018, *A&A*, 614, A122
- Toulis, P. & Bean, J. 2021, *arXiv e-prints*, arXiv:2105.14222
- Tuomi, M., Jones, H. R. A., Barnes, J. R., et al. 2018, *AJ*, 155, 192
- Tuomi, M., Jones, H. R. A., Barnes, J. R., Anglada-Escudé, G., & Jenkins, J. S. 2014, *MNRAS*, 441, 1545
- Udry, S., Mayor, M., Clausen, J. V., et al. 2003, *A&A*, 407, 679
- Wilson, O. C. 1968, *ApJ*, 153, 221
- Yu, J., Huber, D., Bedding, T. R., & Stello, D. 2018, *MNRAS*, 480, L48
- Zechmeister, M. & Kürster, M. 2009, *A&A*, 496, 577

Appendix A: Algorithms available on GitHub

We do not describe here the algorithms (see Sec. 2.3 and 3.2), but rather the contents of the directory available online¹³. This directory contains algorithms written in Python 3.

In the directory “*Func/*”, the user can find

- The implementation of Algorithms 1 and 2.
- A function to evaluate the periodograms \mathbf{p} and $\bar{\mathbf{p}}_L$ involved in Algorithms 1.
- A function to evaluate the detection tests involved in Algorithms 1.
- A file containing functions that implement a set of nuisance signal models \mathcal{M}_d , a function to estimate the parameters θ_d of these models, and a function to generate synthetic data from these models.
- A file containing functions that implement a set of nuisance signal models \mathcal{M}_n , a function to estimate the parameters θ_n of these models, and a function to generate synthetic data from these models.
- A file containing functions that save and read the results of the Algorithms 2’s outputs.

The current release implements the different setting (e.g., periodograms, considered set of frequencies, detection tests, noise models parameters estimation,...) that were used in this work. Further settings will be added in the future (see Table. 1), but the users can already implement their own tools such as:

- new periodograms,
- new detection tests,
- new nuisance component models,
- new parameters estimation procedure,
- new priors laws,
- new stochastic component models.

Note that Algorithms 1 and 2, and the read/save function files do not need to be modified by the user.

As illustration of how to use these released functions, we provide our heavily commented codes that were used to generate the numerical examples presented in Sec. 5.3 and 5.5 of the present paper (see “*Examples 1*” and “*Example 2*”, respectively). The first example implements the case where a null training sample (NTS) of the stochastic noise \mathbf{n} is available. The second example implements the case where no NTS of the stochastic noise \mathbf{n} is available. In this case, the NTS is estimated from the RV series under test.

We plan to improve this current release with new settings, a parallelization scheme, and practical examples of implementation for state-of-the-art RV data analyses in a near future.

Appendix B: Main notations

Table B.1: Table of the main notations used in the paper.

Z, z	Z : Scalar random variable, z : one realization of Z
\mathbf{z}	Vector $[z_1, \dots, z_N]^\top$
$\mathcal{H}_0, \mathcal{H}_1$	Null and alternative hypotheses
\mathbf{x}	Time series under test
\mathbf{s}	RV planet signal under \mathcal{H}_1
\mathbf{n}	Stochastic colored noise of covariance matrix Σ
\mathbf{w}	White Gaussian noise of variance σ_w^2
\mathbf{d}	Nuisance signal
N	Number of data points
\mathcal{T}_L	Null training sample
L	Number of time series available in the NTS
\mathbf{c}	Ancillary time series that can be used to model \mathbf{d}
$\mathcal{M}_s(\theta_s)$	Model of \mathbf{s} depending on parameters vector θ_s
$\mathcal{M}_n(\theta_n)$	Model of \mathbf{n} depending on parameters vector θ_n
$\mathcal{M}_d(\theta_d)$	Model of \mathbf{d} depending on parameters vector θ_d
$\hat{\theta}, \hat{\delta}$	Estimate of parameter vector θ , and perturbation interval of this parameter
π	Parameters’ prior distribution for $\hat{\theta}$ with scale parameter $\hat{\delta}$
ν_k	Frequencies
Ω	Indices set of considered frequencies
\mathbf{p}	Periodogram
$\bar{\mathbf{p}}_L$	Periodogram averaged with L training data sets
$\tilde{\mathbf{p}} \bar{\mathbf{p}}_L$	Periodogram standardized by $\bar{\mathbf{p}}_L$
T_M	Test of the highest periodogram value (“Max test”)
T_C	Test of the N_C^{th} highest periodogram value
(\mathbf{P}, \mathbf{T})	Couple {periodogram, test}
Φ_T	CDF of the considered test statistic T
t	Test statistic
$\{B, b\}$	Number of MC simulations in Algorithm 2
p_v	p -value

¹³ <https://github.com/ssulis/3SD>

Appendix C: Validation of MHD simulations with RV ground-based dataset

The realism of the RV extracted from 3D MHD simulations has been demonstrated in [Sulis et al. \(2020\)](#), by comparing them with spatial RV data taken from the GOLF/SoHO spectrophotometer (see Sec. 2.2.4 and Fig. 2 of [Sulis et al. 2020](#)). In this Appendix, we extend this demonstration to solar ground-based RV data taken with HARPS-N ([Collier Cameron et al. 2019](#), [Dumusque et al. 2021](#)). We selected the $L = 26$ synthetic MHD time series of solar granulation that are described in Sec. 4.2.1, and the 430-days solar time series of HARPS-N. Their estimated power spectral densities are shown in Fig. C.1. We observe a very good match (amplitudes, frequency dependence of the noise) between the PSDs in the period regime where granulation dominates (red horizontal arrow). This example shows that MHD simulations, tuned for the stellar type of a target host star, could be used to provide realistic time series of the stellar granulation noise of this star.

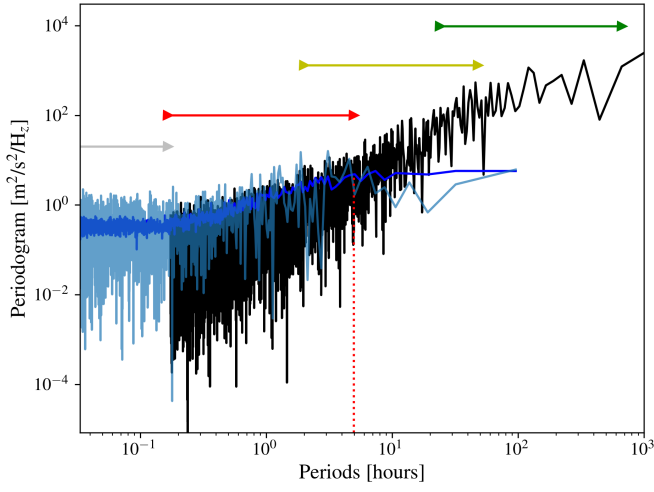


Fig. C.1: PSDs comparison of solar RV taken with the HARPS-N telescope (black, 430 days) and synthetic RV extracted from 3D MHD simulations of solar granulation (light blue, 2 days). The averaged periodogram of the 26 MHD 2-days time series is shown in dark blue. Period ranges dominated by high frequency noises (instrumental and oscillations), granulation, supergranulation and magnetic activity are respectively indicated with the grey, red, yellow and green arrows. The red dotted vertical line indicates the period limit (~ 5 hours) where the PSD is no longer dominated by the granulation noise.